BACHELOR

Modelling of solar cell production

a global model of a microwave hydrogen-silane plasma and the effect of pulsed input power

Berghuis, W.J.H.

Award date:
2015

EINDHOVEN UNIVERSITY OF TECHNOLOGY

Modelling of solar cell production

A global model of a microwave hydrogen-silane plasma and the effect of pulsed input power

Willem-Jan Berghuis
Supervised by dr. ir. Wouter Graef & dr.ir. Jan van Dijk
8-7-2015

Abstract

The goal of this project is to make a global model of a hydrogen-silane coaxial microwave plasma and to investigate the effects of pulsed input power. This is interesting since hydrogen-silane plasmas are used to deposit a thin film of amorphous silicon in, for example, the production of solar cells. For manufacturers it is interesting to know how to control and enhance the deposition. Since the variables to control the plasma are limited, pulsing is an interesting option to investigate. Modeling time dependent processes like pulsing with a conventional 2D-model is extremely time consuming. A global model, however, requires relatively little computational power and is therefore more practical for modelling time dependent processes. The silane model made in this project is based on the self-consistent 2D-model of S.Rahimi. The modelling was carried out using PLASIMO, a plasma modelling platform developed at the Eindhoven University of Technology. Comparison of the global model with this 2D-model showed many similarities. Besides this, we obtained several results for the pulsed power input model.

Contents

1 Introduction 4
2 Zero-dimensional Hydrogen model 6
2.1 Introduction 6
2.2 Model 6
2.2.2 Species and volume reactions 7
2.2.3 Wall reactions 8
2.2.4 Analytic transport model 9
2.2.5 Numerical transport model 11
2.2.6 Power-Input 16
2.3 Results and discussion 16
2.3.1 Comparison of the ion fluxes in the analytic and numerical model 16
2.3.2 The influence of the hydrogen wall recombination probability 17
2.3.3 Comparison of the analytic and numerical model with the 2D-model 18
2.3.4. Results of modelling the inner 4.5% of the volume 22
2.3.5 Comparison of the 2D-model with experiments 23
2.4 Conclusion 25
3 Zero-dimensional Hydrogen-Silane model 26
3.1 Introduction 26
3.2 Model 26
3.2.1 Species and volume reactions 26
3.2.2 Wall reactions 26
3.3 Results and discussion 30
3.3.1 Comparison between the global model and the 2D-model 30
3.3.2 Influence of the hydrogen recombination probability on the deposition rate 33
3.3.3 Influence of the input power on the deposition rate 34
3.4 conclusion 35
Extension final Bachelor project 36

4 Pulsed power input 37
4.1 Introduction 37
4.2 Pulsed power input 37
4.3 Results and discussion 38
4.3.1. Pulsed hydrogen plasma 38
4.3.2 Pulsed hydrogen-silane plasma 41
4.4 Conclusion 46
References 47

1 Introduction

The goal of this project is to make a global model of hydrogen-silane coaxial microwave plasma and to investigate the effects of pulsed input power. The reason for this has to do with the silicon deposition in silane plasmas. In a silane plasma all kinds of reactive silane radicals are formed and these can interact with the surface to form a thin film of amorphous silicon. The name of this technique is called Plasma Enhanced Chemical Vapor Deposition (PECVD) and it is used in, for example, the production of solar cells. For manufacturers it is interesting to know how to control and enhance the deposition. There are a few variables they can change to control the deposition. They can for example change the plasma pressure or the magnitude of the input power. Not only can the magnitude of the input power be changed, also its time dependency. For example, pulsed input power can be applied instead of a constant power supply. Since the variables to control the plasma are limited, this is an interesting option to investigate. Modeling time dependent processes like pulsing is demanding for a conventional 2D-model. It takes already days to convert a two-dimensional steady state model, so this is not a practical solution. A global model however takes very little computational power and is therefore able to handle time dependent processes. For this reason a global model is built.

We started the project building a global model for microwave hydrogen plasma. This is done in PLASIMO [22], plasma modelling software developed by the applied physics department of Eindhoven University of Technology. The reason for starting with a hydrogen model is the fact that there was literature available about global hydrogen models. From several papers, formulas and background information could be extracted. We could also make a comparison with these papers. The hydrogen model served therefore as base for the hydrogen-silane model. The silane model makes use of the same principles and the same modelling software as the hydrogen model and was therefore finished pretty soon after the hydrogen model. During the last weeks of the project, pulsing was investigated (as extension of the final bachelor project). Pulsing was applied to both the hydrogen and silane plasma and the effects were investigated.

For the same plasma configuration as used in this project (see figure 1), Sara Rahimi made a self-consistent two-dimensional model [1]. This model is far more complex than the global model, however it takes days to converges and is therefore not able to investigate pulsing. Her model and her thesis formed the base of our global model. We tried to stay as close as possible to her model. One might say we converted the two-dimensional model to a zero-dimensional model. The results of both models are discussed and compared in the result sections.

This report starts with a chapter about the hydrogen model. This chapter is used to explain the working of the global model we built. The chapter ends with a section about the results of the model and a comparison of these results with the results of S. Rahimi. The next chapter describes the silane model. Since this model is based on the hydrogen model, only the differences are discussed. The

chapter ends with the results of the model. The last chapter is about the effect of pulsed input power. A small introduction tells something about the used pulses and then the effect of pulsing on the deposition rate are shown. Like the other two chapters, there is a short conclusion at the end.

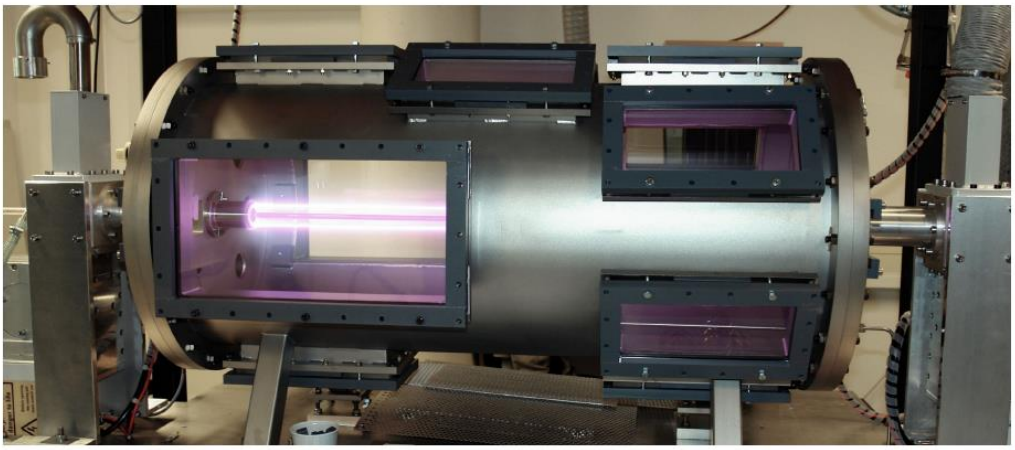

Figure 1.Picture of the coaxial plasma setup. The plasma is confined in a vessel with a radius of 10 cm and a length of 50 cm. At the center of the vessel there is a metal bar surrounded by a quartz tube. The microwaves are sent into the vessel through the quartz tube. As one can see the plasma is mainly positioned around the quartz tube [15].

2 Zero-dimensional Hydrogen model

2.1 Introduction

The aim of this section is to create a zero-dimensional model of a hydrogen plasma discharge in a coaxial microwave that will act as base for a hydrogen-silane model. The zero-dimensional hydrogen model itself is based on a two-dimensional model of this coaxial microwave made by S. Rahimi [1]. The plasma is modeled in PLASIMO.

2.2 Model

2.2.1 Geometry

The geometry of the system can be seen in figure 2 and 3. The center of system consists of a metal bar with a radius of 3.65 mm (depicted as a black dot in figure 2). The metal bar is surrounded by a quartz tube (R_0-R_i). Between the quartz tube and the metal rod is air at atmospheric pressure. The plasma is located around the quartz tube and confined by a metal layer at R. The reactor has a length Z_T=500 mm.

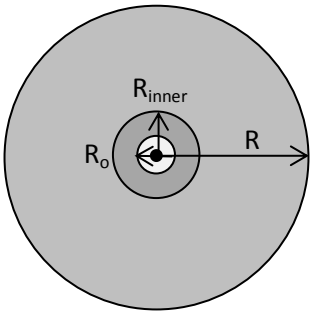

Figure 2. Geometry of the system [1]. R=100 mm, R_i=15 mm, R_0=13 mm, Z_T=500 mm.

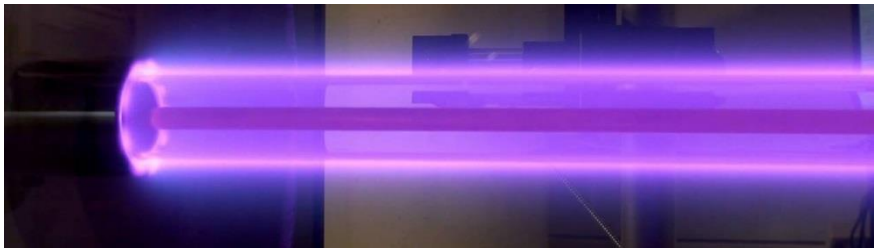

Figure 3. Geometry of the system.

2.2.2 Species and volume reactions

The hydrogen plasma is created by sending microwaves into a hydrogen gas. The microwaves form energetic electrons, which can collide with the hydrogen molecules. The collision can cause ionization and disassociation of the hydrogen molecule. Due to these inelastic collisions species like H, H^+, H_2^+ and H_3^+ are formed. Besides ionization or disassociation, a collision can also cause vibrational excitation of the hydrogen molecule. In Rahimi's model only the level 4 vibrational state $H_2^{v=4}$ is taken into account. The reason for this is its role in the charge exchange reaction: $H_2^{v=4} + H^+ \rightarrow H_2^+ + H^+$, since the energy of the excited state is approximately the same as the energy difference between H^+ and H_2^+. We mimic the model of Rahimi, so the global model contains only the level 4 vibrational state of hydrogen. Higher vibrational levels are neglected in this model. Besides inelastic collisions, there are of course elastic collisions, but these collisions cause only a redistribution of translational energy. An overview of the reactions can be found in table 1.

#	Reaction	Reaction rate coefficient $K_r(T)$	Ref.
1	$H_2 + e \leftrightarrow H_2^+ + 2e$	$1.58 \cdot 10^{-14}\, T_e^{0.5} e^{-\frac{15.378}{T_e}}$	[6]
2	$H_2 + e \leftrightarrow 2H + e$	$1.413 \cdot 10^{-15}\, T_e^{2} e^{-\frac{4.48}{T_e}}$	[6]
3	$H + e \rightarrow H^+ + 2e$	$1.914 \cdot 10^{-14}\, T_e^{0.758} e^{-\frac{9.56}{T_e}}$	[6]
4	$H_2^+ + e \rightarrow H^+ + H + e$	$6.8 \cdot 10^{-15} T_e^{1.571} e^{-\frac{2.7}{T_e}}$	[6]
5	$H_3^+ + e \rightarrow H_2 + H$	$9.7 \cdot 10^{-14} T_e^{-0.5}$	[7]
6	$H_2^+ + e \rightarrow 2H$	$5.66 \cdot 10^{-14} T_e^{-0.5}$	[7]
7	$H^+ + e \rightarrow H$	$2.62 \cdot 10^{-19} T_e^{-0.5}$	[7]
8	$H_2^+ + H_2 \rightarrow H_3^+ + H$	$2.1 \cdot 10^{-15}$	[8]
9	$H_2 + H \leftrightarrow 3H$	$5.6 \cdot 10^{-15} T_{H_2}^{0.419} e^{-\frac{4.478}{T_{H_2}}}$	[8]
10	$2H_2 \leftrightarrow 2H + H_2$	$5.6 \cdot 10^{-15} T_{H_2}^{0.419} e^{-\frac{4.478}{T_{H_2}}}$	[8]
11	$H_2 + e \leftrightarrow H_2^{v=4} + e$	$4.69 \cdot 10^{-16} T_{H_2}^{0.8202} e^{-\frac{1.89}{T_{H_2}}}$	[8]
12	$H_2^{v=4} + H^+ \rightarrow H_2^+ + H$	$2.5 \cdot 10^{-15}$	[8]

Table 1. Overview of the volume reactions

A reaction *r* from table 1, can be described more generally with

$$\sum_s v_{s,r}^d X_s^d \rightarrow \sum_s v_{s,r}^p X_s^p \quad , \tag{1}$$

where X_s^d stands for species *s* before the reaction and X_s^p stands for species *s* after the reaction. The amounts of species *s* before and after the reaction *r,* are given by the stoichiometric coefficients $v_{s,r}^d$ and $v_{s,r}^p$ respectively [3]. The summation in (1) runs over all the species. For species that are not involved the stoichiometric coefficient is simply zero.

The frequency at which a reaction *r* takes place can also be described in a general way:

$$R_r = K_r(T) \prod_s n_s^{v_{s,r}^d}, \tag{2}$$

with $K_r(T)$ the reaction rate coefficient given by table 2 [3]. The product in this formula runs over all the species. For species that are not involved, $v_{s,r}^d$ is zero again. The zero-dimensional model has to predict the densities of the species H, H^+, H_2^+, H_3^+, $H_2^{v=4}$,H_2 and e. In order to do so, the model needs expressions for the net production of each species. Since we have just found expression for the reactions and their frequency, we are able to define net production of each species:

$$S_s = \sum_r \left(v_{s,r}^p - v_{s,r}^d\right) R_r = \sum_r \left(v_{s,r}^p - v_{s,r}^d\right) K_r(T) \prod_s n_s^{v_{s,r}^d}. \tag{3}$$

For each reaction the net production of a species equals the amount of species s after the reaction ($v_{s,r}^p$) minus the amount of species *s* before the reaction ($v_{s,r}^d$) times the frequency of the reaction R_r. By performing a summation over all the reactions, we obtain the total net production S_s of species *s*.

2.2.3 Wall reactions

Particles in the plasma can not only collide with other particles in the plasma, but also with the quartz or metal wall. When an ion like H^+ hits the wall, it picks up an electron and becomes neutral. The rate of these processes is determined by the flux of the ions at the wall. Rahimi calculated this flux with

$$\Gamma_A = n_{s,A} v_B = n_{s,A} \sqrt{\frac{k_B T_e}{m_A}} \tag{4}$$

where $n_{s,A}$ is the density of ion A at the sheath edge, $v_B$the Bohm velocity, k_B the Boltzmann constant, T_e the electron temperature and m_A the mass of ion A [1,2,4]. Since a global model only involves a mean density, we need to relate the sheath edge density with the bulk or mean density. We have done this in two different ways. In the first way, we made use of the analytical obtained relation between the sheath edge density and the bulk density by Godyak and Maximov [5]. In the second way, we used the results of the two-dimensional model of S. Rahimi. Both options will be described and compared in this chapter.

Two other types of wall relations that take place are the de-excitation of vibrationally excited hydrogen $H_2^{v=4}$ and recombination of two hydrogen atoms H to one hydrogen molecule H_2. The rates at which this reaction take place can be described with an analytic diffusion relation or they can be described by using the results of the two-dimensional model. Just like the ion-wall interactions both will be discussed in the next two sections.

2.2.4 Analytic transport model

One way to obtain a relation between the sheath edge density and the bulk or mean density is to use the relation obtained by Godyak and Maximov. They calculated this relation for cylindrical radio frequency plasma reactor. Although the reactor in this chapter is coaxial and the frequency of the power supply is not in the RF-region, we assume that their calculations are still a good approximation, since the radius of the inner tube (15 mm) is relatively small compared to the radius of the outer tube (100 mm) and because of lack of any other analytic expression for microwave plasmas. In the results section a more detailed discussion can be found about the validity of the expression.

According to Godyak and Maximov [5] the density at the axial sheath edges $n_{sL,A}$ is given by

$$n_{sL,A} = \frac{0.86\, n_{s,A}}{\sqrt{3 + \frac{L}{2\lambda_i}}} \tag{5}$$

and at the radial sheath edge $n_{sR,A}$ is given by

$$n_{sR,A} = \frac{0.80\, n_{s,A}}{\sqrt{4 + \frac{R_o}{2\lambda_i}}} \tag{6}$$

with L the length of the cylinder, R_0 the radius of the outer cylinder and λ_i the ion-neutral collision mean free path given by

$$\lambda_i = \frac{1}{n_{neutral}\, \sigma_i}\,. \tag{7}$$

In this equation $n_{neutral}$ stands for the density of the neutral particles and σ_i stands for the ion-neutral cross section with a value of $\sigma_i = 5 \cdot 10^{-19} m^2$[19]. The total flux of ion A at the wall is subsequently

$$\Gamma_{tot,A} = v_B\left(2\pi({R_o}^2 - {R_i}^2) n_{sL} + 2\pi(R_o + R_i) L n_{sR}\right), \tag{8}$$

with v_B the Bohm velocity given by equation (4), R_i the radius of the inner quartz tube and n_{sL} and n_{sR} given by equation (5) and (6). The ion neutralization probability equals 1, so the ion flux at the wall equals the ion neutralization rate: $R_{neutralization} = \Gamma_{tot,A}$. It is important to note that the electron temperature the Bohm velocity is approximated by the electron temperature of the bulk instead of the electron temperature at the wall. This approximation is made due to lack of an analytic expression for the relation between the electron temperature at the wall and in the bulk.

The reaction rate of the de-excitation of vibrationally excited hydrogen $H_2^{v=4}$ is different from the ion-neutralization reaction rate since it is a neutral particle. For neutral particles the wall reaction rate is determined by diffusion:

$$\mathrm{R}_{\mathrm{de-excitation}} = \Gamma_{H_2^{v=4}} = \frac{D_{eff}}{\Lambda^2} n_{H_2^{v=4}}, \tag{9}$$

where D_{eff} is the diffusion coefficient, Λ the diffusion length and $n_{H_2^{v=4}}$ the concentration of $H_2^{v=4}$ [2]. The diffusion length is a length that characterize the system. For this system the diffusion length is chosen to be the volume divided by the total surface [4]. Another expression for the diffusion length is given by S. Ashida et al. [2]:

$$\frac{1}{\Lambda^2} = \left(\frac{\pi}{L}\right)^2 + \left(\frac{2.405}{R}\right)^2, \tag{10}$$

where Λ is the diffusion length, L the height of the cylinder and R the outer radius of the cylinder. Calculating both expressions gives similar lengths: 3.26 cm and 3.64 cm respectively. The volume divided by the total surface seems therefore a proper choice.

The effective diffusion coefficient in equation (8) is defined as

$$\frac{1}{D_{eff}} = \frac{1}{D_{kn}} + \frac{1}{D_{AB}}. \tag{11}$$

In this expression D_{kn} stands for the diffusivity for Knudsen diffusion and is equal to

$$D_{kn} = \frac{1}{3} \Lambda v_{th}, \tag{12}$$

with Λ the diffusion length and v_{th} the thermal velocity [4]. For the pressures used in this coaxial plasma, the contribution of Knudsen diffusion is minimal, since $Kn \gg 1$. The diffusion is therefore mainly determined by the other diffusion coefficient, D_{AB} , which account for the diffusion of species A in a background gas B. In this case the background gas is molecular hydrogen. The value of D_{AB} is calculated using the Chapman-Enskog equation [21]:

$$D_{AB} = \frac{0.001858\, T^{\frac{3}{2}} \sqrt{\frac{M_A + M_B}{M_A M_B}}}{P \sigma_{AB}^2 \Omega_D}, \tag{13}$$

where T is the temperature in kelvin, M_A and M_B the molar masses, P the pressure in atmosphere, σ_{AB} is equal to $0.5(\sigma_A + \sigma_B)$ with σ_A and σ_B the cross sections of the species in Å and Ω_D the collision integral (no dimension) that can be obtained from a table [21].

A third reaction that occurs at the wall is the recombination of two hydrogen atoms H to one hydrogen molecule H_2. The rate of this reaction is similar to (8):

$$\mathrm{R}_{\mathrm{recombination}} = \gamma_H \, \Gamma_H = \gamma_H \, \frac{D_{eff}}{\Lambda^2} n_H, \tag{14}$$

with γ the recombination probability. This recombination probability is different for the steel wall and the quartz wall. In order to obtain one γ_H for the whole system, the recombination probability is

averaged with the surface of the quartz and metal wall as weight factors. Unfortunately, literature is not clear about the value of γ_H. For the steel wall γ_H differs from 0.004 to 0.2 and for the quartz wall values are given between 0.0001 and 0.001. The recombination probability is therefore taken as a parameter, further investigated in the section 2.3.2. A summary of the analytically obtained wall reactions can be found in table 2.

#	Reaction	Reaction rate
1	$H \rightarrow \frac{1}{2}H_2$	$\mathrm{R}_{Recombintion} = \gamma_H \frac{D_{eff}}{\Lambda^2} n_H$
2	$H_2^{v=4} \rightarrow H_2$	$\mathrm{R}_{\mathrm{de-excitation}} = \frac{D_{eff}}{\Lambda^2} n_{H_2^{v=4}}$
3	$H^+ \rightarrow H$	$R_{neutralization} = v_B\left(2\pi({R_o}^2 - R_i^2)n_{sL} + 2\pi(R_o + R_i)Ln_{sR}\right)$
4	$H_2^+ \rightarrow H_2$	$R_{neutralization} = v_B\left(2\pi({R_o}^2 - R_i^2)n_{sL} + 2\pi(R_o + R_i)Ln_{sR}\right)$
5	$H_3^+ \rightarrow H + H_2$	$R_{neutralization} = v_B\left(2\pi({R_o}^2 - R_i^2)n_{sL} + 2\pi(R_o + R_i)Ln_{sR}\right)$

Table 2. Overview of the wall reactions.

2.2.5 Numerical transport model

The second way to obtain a relation between the sheath edge density and the bulk or mean density is to use the results of the two-dimensional model of S. Rahimi. In the model, the ion density at the wall is the density in the cell adjacent to the wall. By averaging the densities of all these cells, one obtains an averaged value for ion density at the wall: $n_{i_{wall}}$. By taking the average over all cells one gets a mean ion-density over all the volume: $n_{i_{average}}$. By dividing the mean density at the wall by the mean density of the volume, a ratio is found between the density at the wall and the bulk density. The same can be done for the electron temperature. Substituting these ratios in (4) gives the neutralization rate for ion A:

$$\Gamma_A = \left(\frac{n_{i_{wall}}}{n_{i_{average}}}\right) n_{A_{global}} \sqrt{\frac{k_B\left(\frac{T_{e_{wall}}}{T_{e_{average}}}\right) T_{e_{global}}}{m_A}} = C_A\, n_{A_{global}} \sqrt{T_{e_{global}}}\,, \tag{15}$$

where $n_{A_{global}}$ is the density of A in the global model, $T_{e_{global}}$ is the electron temperature in the global model and C_A is a constant defined as

$$C_A = \left(\frac{n_{i_{wall}}}{n_{i_{average}}}\right) \sqrt{\frac{k_B\left(\frac{T_{e_{wall}}}{T_{e_{average}}}\right)}{m_A}}. \tag{16}$$

Relation (14) can be obtained for each of the four walls in the coaxial reactor: the quartz wall at R_i, the metal wall at R_o, the bottom and top of the reactor. The total flux or neutralization rate of ion A becomes:

$$R_{neutralization,A} = \pi({R_o}^2 - R_i^2)(\Gamma_{top,A} + \Gamma_{bottom,A}) + 2\pi L(R_o\Gamma_{R_o,A} + R_i\Gamma_{R_i,A}). \tag{17}$$

By substituting expression (14) for the fluxes, one can separate the variables from the constants and write a simplified version of (16):

$$R_{neutralization,A} = C_{tot,A}\, n_{A_{global}} \sqrt{T_{e_{global}}}\,. \tag{18}$$

In this expression (17) $C_{tot,A}$ is defined as

$$C_{tot,A} = \pi({R_o}^2 - R_i^2)(\mathrm{C}_{t,A} + \mathrm{C}_{bottom,A}) + 2\pi L(R_o \mathrm{C}_{R_o,A} - R_i \mathrm{C}_{R_i,A}). \tag{19}$$

The calculated values for the flux constant $C_{tot,A}$ are given in table 3 on the next page. For H^+ and H_2^+ an increasing flux constant is observed when the plasma pressure rises. The flux constant of H_3^+ is more or less constant compared to the other two ions. This behavior can be related to the radial distribution of the ions. When we look at the radial distribution in figure 4, we see that for higher pressure, the plasma moves towards the inner quartz tube. As a consequence of this, the density directly at the quartz wall (r=0.015 m) increases, leading to a higher ion flux and therefore it contributes to a higher flux constant. Important is the observation that the ion-flux is nearly totally determined by the flux towards this inner wall. For example the flux of H^+ at 1.4 mbar: C_A at the inner wall is $2.1{\cdot}10^3\ m^3 s^{-1} K^{-0.5}$ and for the outer wall C_A is only $0.0014\ m^3 s^{-1} K^{-0.5}$! The increasing density at the inner wall does therefore not only contribute to a higher flux constant, but actually determines the flux constant. The radial distribution of H_3^+, does not show large difference as pressure rises, as a consequence the flux constant remains relatively constant.

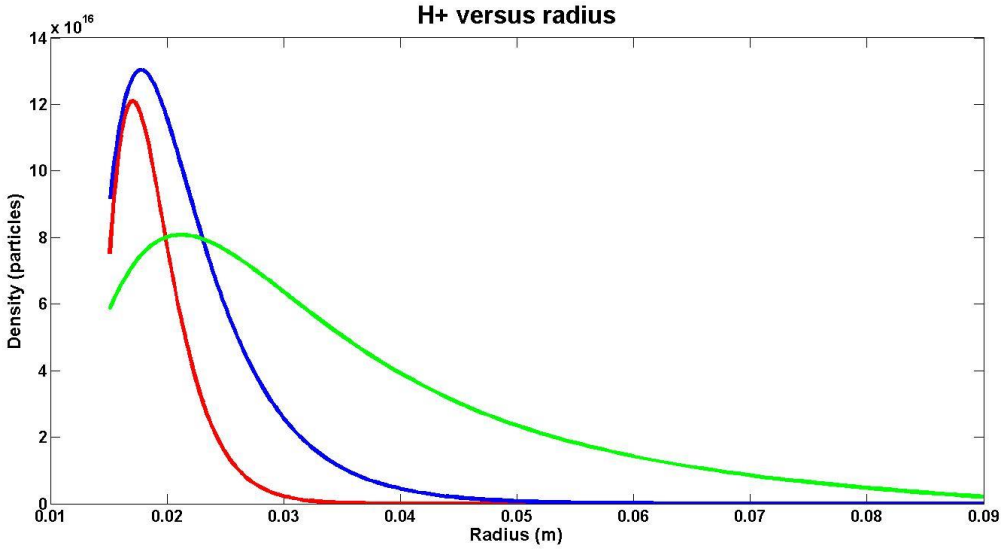

Figure 4. The radial density distribution of H^+ as function of pressure. The green line is the density of H^+ for 0.1 mbar, the blue line depicts the density of H^+ at 0.8 mbar and the red line shows the distribution of H^+ at 2 mbar. As one can see, the plasma moves towards the center of the coaxial vessel (left) when pressure increases. The latter results in higher flux constant for H^+. Furthermore one can see that the density at the inner wall (0.015 m) is much larger than the density at the outer wall (0.09 m). The total flux is therefore practically determined by the flux to the inner wall.

Pressure $(mbar)$	C_{tot}, H^+ $(m^3 s^{-1} K^{-0.5})$	C_{tot}, H_2^+ $(m^3 s^{-1} K^{-0.5})$	C_{tot}, H_3^+ $(m^3 s^{-1} K^{-0.5})$
0.1	6.2e+02	1.0e+03	5.5e+02
0.2	5.5e+02	1.4e+03	4.0e+02
0.8	1.5e+03	4.1e+03	4.1e+02
1.4	2.1E+03	4.4E+03	4.3e+02
2	2.4e+03	4.1e+03	4.2e+02

Table 3. Overview of the flux constants obtained from the two-dimensional model. The flux constants of H^+ and H_2^+ increase with pressure and flux constant of H_3^+ is more or less constant compared to the other two ions.

A similar calculation can be done for the neutral-wall interactions. The flux of particles to the wall can be described by

$$\Gamma_A = \frac{1}{4} v_{th,A} n_A = \frac{1}{4} n_A \sqrt{\frac{8 k_B T_e}{m_A}}, \tag{20}$$

with $v_{th,A}$ the thermal velocity of particle A and n_A the density of particle A at the wall, k_B is the Boltzmann constant, T_e the electron temperature and m_A the mass of ion A [14]. For the density at the wall the same method is used as for the ion density. Consequently the flux of neutral particles equals

$$\Gamma_A = \frac{1}{4} \gamma \left(\frac{n_{n_{wall}}}{n_{n_{average}}} \right) n_{A_{global}} \sqrt{\frac{8 \, k_B \left(\frac{T_{e_{wall}}}{T_{e_{average}}} \right) T_{e_{global}}}{m_A}}, \tag{21}$$

with γ the reaction probability. Like equation (16), this equation can be calculated for all for walls in order to get an expression for the total flux.

$$C_{neutralization,A} = \pi (R_o^2 - R_i^2)(\gamma_{top} \Gamma_{top,A} + \gamma_{bottom} \Gamma_{bottom,A}) + 2\pi L (\gamma_o \mathrm{R_o} \Gamma_{R_o,A} - \gamma_i R_i \Gamma_{R_i,A}). \tag{22}$$

Equation (22) can be simplified performing the same simplification as (17):

$$C_A = C_{tot,A} \, n_{A_{global}} \sqrt{T_{e_{global}}} \, . \tag{23}$$

For the de-excitation of vibrational excited hydrogen all γ equals 1. For the recombination of atomic hydrogen to molecular hydrogen $\gamma_o = \gamma_{top} = \gamma_{bottom} = \gamma_{metal}$ and $\gamma_i = \gamma_{quartz}$. Although literature is not clear about the values of γ_{metal} and γ_{quartz} ,for the rate coefficients in table 4, 0.1 and 0.001 are used respectively. An overview of all wall reactions is placed in table 5. The values for the flux constant C_A of the neutral particles can be found in table 4.

Pressure (mbar)	C_{tot} , H $(m^3 s^{-1} K^{-0.5})$	C_{tot} , $H_2^{v=4}$ $(m^3 s^{-1} K^{-0.5})$
0.1	70	4.0e+02
0.2	44	2.8e+02
0.8	7.3	1.9e+02
1.4	13	1.8e+02
2	8.6	1.4e+02

Table 4. Overview of the wall-bulk ratios obtained from the two-dimensional model. Although the density of $H_2^{v=4}$ increases at the walls for higher pressure, the flux constant of $H_2^{v=4}$ decrease. This can be explained by the fact that the average density of the $H_2^{v=4}$ rises even more, resulting in a decrease of the flux constant. You can see this in figure

The flux constant of $H_2^{v=4}$ is decreasing with pressure, the opposite of the ion flux constants. Although the density of $H_2^{v=4}$ at the wall increases, the average density shows an increase as well, resulting in a decrease of the flux constant. This can be seen in figure 5 or in figure 14.2 of the result section. The latter is more obvious. Concerning the flux constant of the atomic hydrogen, no clear trend can be found. From figure 6 it follows that the flux increases with increase of pressure, however from the flux constant no such thing can be derived. The values of the flux constant become very small for pressure of 0.8 mbar and higher. Keeping this in mind, one can argue that the differences at these pressures are caused by approximations and small computational errors in the script that calculates the flux constants. These small differences are present at all calculated fluxes, but now visible due to the very small values of the fluxes. In this case a decrease in flux constant is observed, just like the flux constant of $H_2^{v=4}$.

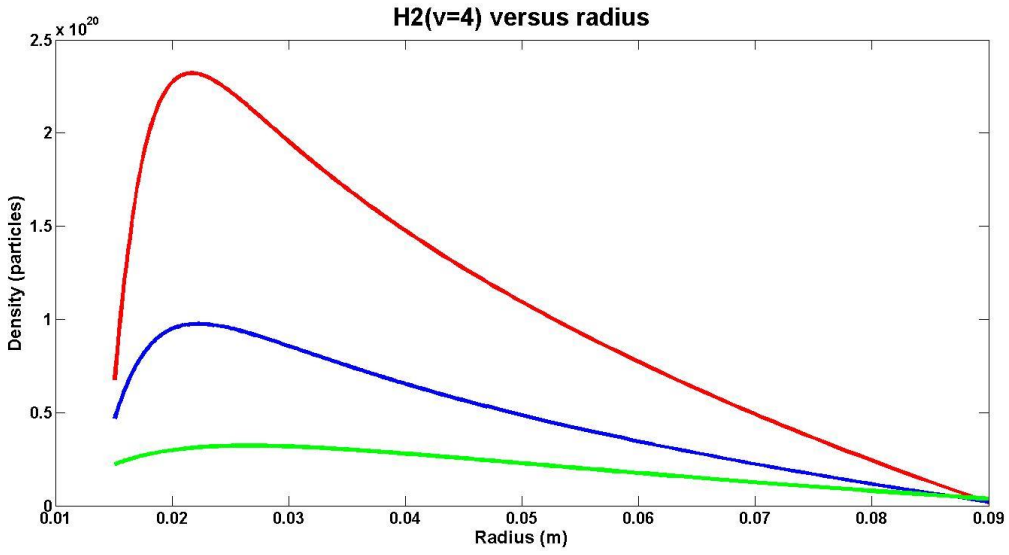

Figure 5. The radial distribution of $H_2^{v=4}$. The green line shows the density of $H_2^{v=4}$ at 0.2 mbar, the blue line depicts 0.8 mbar and the red one 2 mbar. An increase of the density at the quartz wall (0.015 m) can be seen as well as the large difference intensity compared to the outer wall (0.09 m). One can also see that the total average density increase since the density increase at each radial position. For $H_2^{v=4}$ the same applies as for the ions: the flux is nearly 100% determined by the flux to the inner wall.

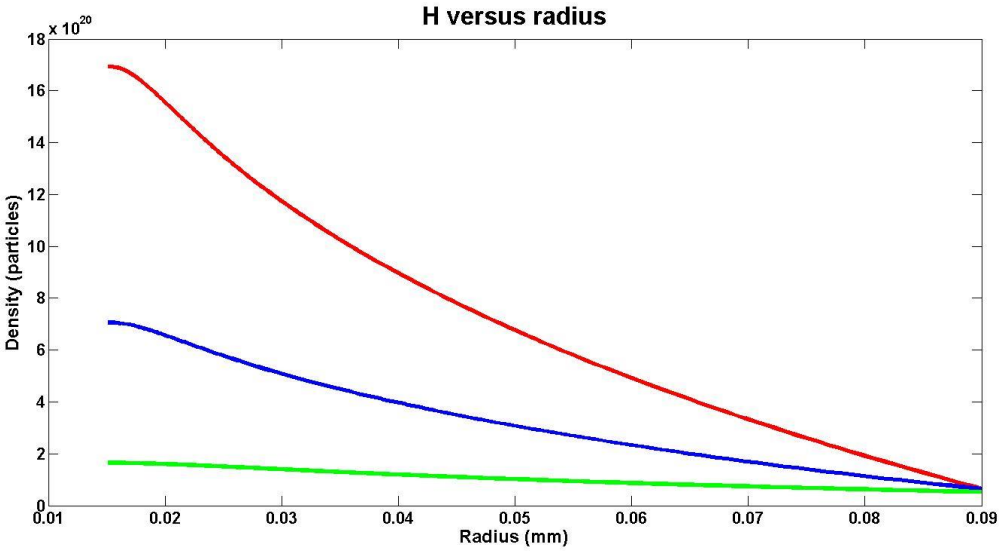

Figure 6. The radial distribution of atomic hydrogen. The green line shows the density of H at 0.2 mbar, the blue line depicts 0.8 mbar and the red one 2 mbar.

#	Reaction	Reaction rate
1	$H \rightarrow \frac{1}{2}H_2$	$\mathrm{R}_{Recombintion} = C_{tot,H}\, n_{H_{global}} \sqrt{T_{e\,global}}$
2	$H_2^{v=4} \rightarrow H_2$	$\mathrm{R}_{de-excitation} = C_{tot,H_2^{v=4}}\ n_{H_2^{v=4}\,global} \sqrt{T_{e\,global}}$
3	$H^+ \rightarrow H$	$R_{neutralization} = C_{tot,H^+}\ n_{H^+\,global} \sqrt{T_{e\,global}}$
4	$H_2^+ \rightarrow H_2$	$R_{neutralization} = C_{tot,H_2^+}\, n_{H_2^+\,global} \sqrt{T_{e\,global}}$
5	$H_3^+ \rightarrow H + H_2$	$R_{neutralization} = C_{tot,H_3^+}\ n_{H_3^+\,global} \sqrt{T_{e\,global}}$

Table 5. Overview of the wall reactions

2.2.6 Power-Input

The power input of the real hydrogen discharge comes from the electromagnetic microwaves with a frequency of 2.45 GHz that are sent into the plasma. In this model, the power input is modeled as a constant absorbed power per plasma volume. The fraction of the power that is absorbed from the 1500 W power input is taken from the results of the two-dimensional model of S. Rahimi. An overview of the absorbed power as function of pressure can be found in table 6.

Pressure (mbar)	Fraction absorbed power
0.1	0.614
0.2	0.643
0.8	0.818
1.4	0.94
2	0.97

Table 6. Overview of the absorbed power as function of pressure

2.3 Results and discussion

2.3.1 Comparison of the ion fluxes in the analytic and numerical model

In the analytic transport model the equations (5) and (6) of Godyak and Maximov were used to obtain a relation between the sheath edge density and the bulk or mean density. In the numerical transport model we derived this relation from the two-dimensional model, using the average density of each ion as bulk density. A comparison of these two methods can be found in the following figures (7,8). In the figures the axial and radial sheat edge density are given as fraction of the bulk density. This is done for different pressure ranging from 0.1 mbar to 2 mbar. The relation of Godyak and Maximov is not ion-specific: the relation is the same for all ions. From the 2D-model however, different relation could be obtained for each different ion (H^+, H_2^+ and H_3^+). The latter appeared to be important since the ratios of the three ions show major differences, especially the ratio of the H^+ and H_2^+ ion. In the axial sheat edge density fraction of figure 7 for example, the H+ ion shows an opposite trend from Godyak and Maximov and from the other ions. Maybe this is because of its small size. In the radial sheat edge density graph, the H_2^+ ion is the one with most deviation from the Godyak and Maximov result. Although the ion shows a similar trend, its absolute value is much lower. The only ratio that is in reasonable agreement with the Godyak and Maximov result is the H_3^+ ion. Since this ion forms the majority of the ions, it is this ion that has the largest impact on the electron density and therefore on the plasma. The fact that the volume relations are dominant and the fact that the H_3^+ ion has similar wall densities for both transport models leads to very small difference between the two global models.

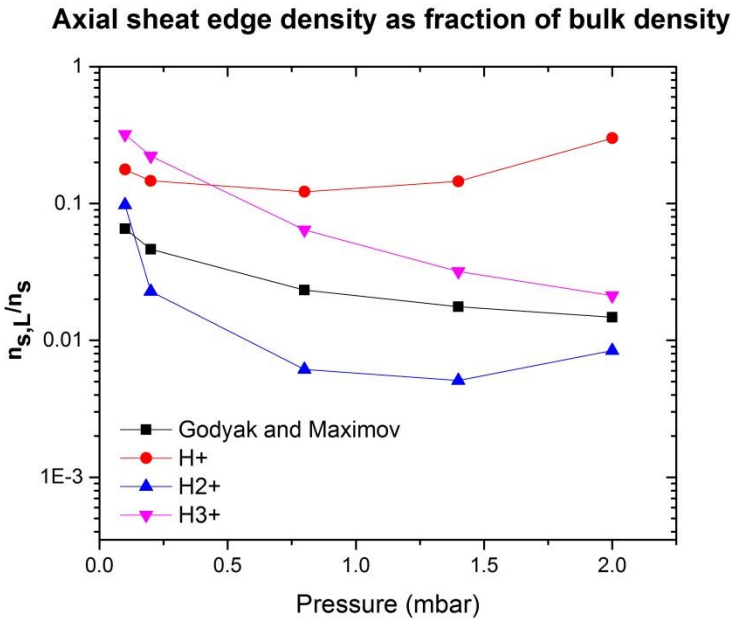

Figure 7. Axial sheat edge density $n_{s,L}$ as fraction of the bulk density n_s. There is a significant difference between the ratio of Godyak and Maximov and the ratio obtain from the 2D-model of S. Rahimi. Another important observation is the difference in ratios between the different ions.

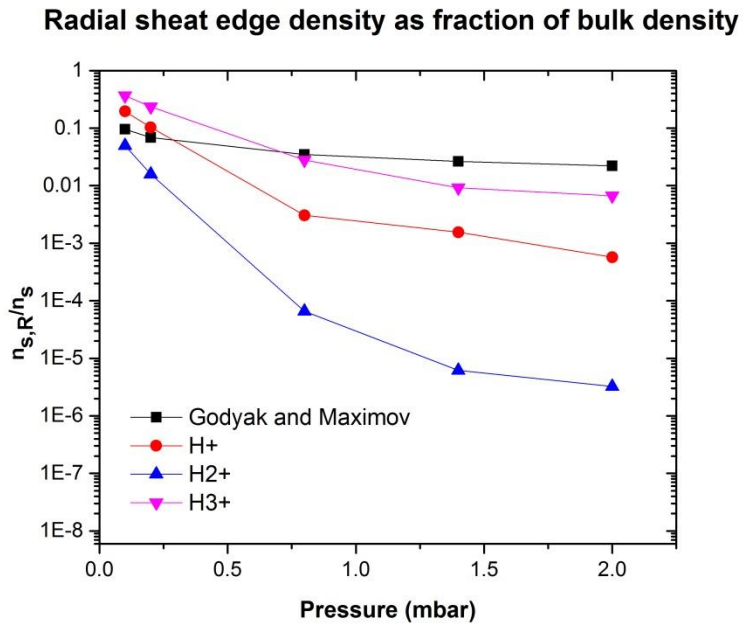

Figure 8. Radial sheat edge density $n_{s,R}$ as fraction of the bulk density n_s.

2.3.2 The influence of the hydrogen wall recombination probability

In section 2.2.4. it was mentioned that literature is not clear about the value of the wall recombination probability of hydrogen. In this section the influence of the recombination probability

on the hydrogen density and ion density is therefore investigated. The recombination probability of metal is changed from 0 to 0.2, the highest value reported in literature. The recombination probability of quartz is changed from 0 to 0.001. This was done at a pressure of 0.8 mbar with the analytic model. Changing the recombination probability of quartz showed no significant differences in densities. This is supported by the hydrogen fluxes obtained from the 2D-model. The flux to the quartz wall is only 10% of the flux to the metal wall. Changes in the quartz recombination are therefore likely to have a relatively small impact. The change of the metal recombination probability shows however large differences. The hydrogen density changed by a factor 45. For the ions the change is smaller: a factor 2.7. This can be seen in figure 9. The magnitude of the recombination probability is important for the modeling results and for reliable results the right recombination probability should be carefully investigated.

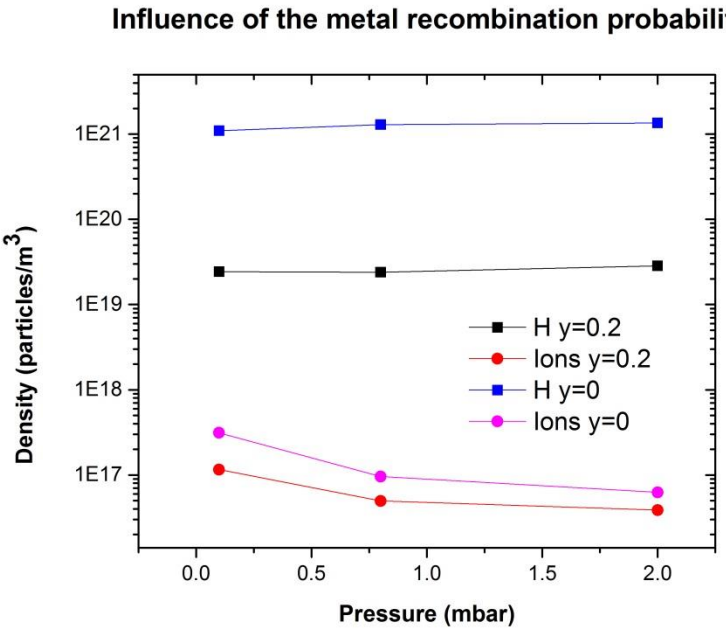

Figure 9.The influence of the metal recombination probability on the hydrogen and ion density. The simulations were performed with a pressure of 0.8 mbar.

2.3.3 Comparison of the analytic and numerical model with the 2D-model

In figure 10 and 11 the properties of the electrons are displayed. The electron density and electron temperature of the analytic, numerical and 2D-model are plotted against the pressure. The trend and absolute values of the electron temperature are in good agreement with the 2D-model. This is also the behavior one could expect. By increasing the pressure, the densities increases and hence the collision frequency will rise. Since the input power remains the same, the increased collision frequency will cause the electrons to lose more energy and hence to have a lower electron temperature. Unlike the electron temperature, the electron densities of the global models show only similarities with the 2D-model above 0.8 mbar. Below this pressure an opposite trend is observed. Since the electron density is calculated using quasi-neutrality, this behavior is caused by the density behavior of the ions. The majority of the ions is formed by H_3^+ and the trend of this ion is indeed similar, see figure 12. The discrepancy of H_3^+ between models at 0.1 and 0.2 mbar is related to the

differences in electron temperature for these pressures. For higher pressures, the trends of the electron temperature are the same, but at lower pressures the temperature of the global models remains relatively low. This causes a smaller destruction of H_3^+ in the volume reaction 5 of table 1: $H_3^+ + e \rightarrow H_2 + H$ with rate $9.7 \cdot 10^{-14} T_e^{-.05}$. The result of this lower destruction is a larger density of H_3^+ for the global models at low pressures. At higher pressures the electron temperature trends are similar and so are the trends of H_3^+.

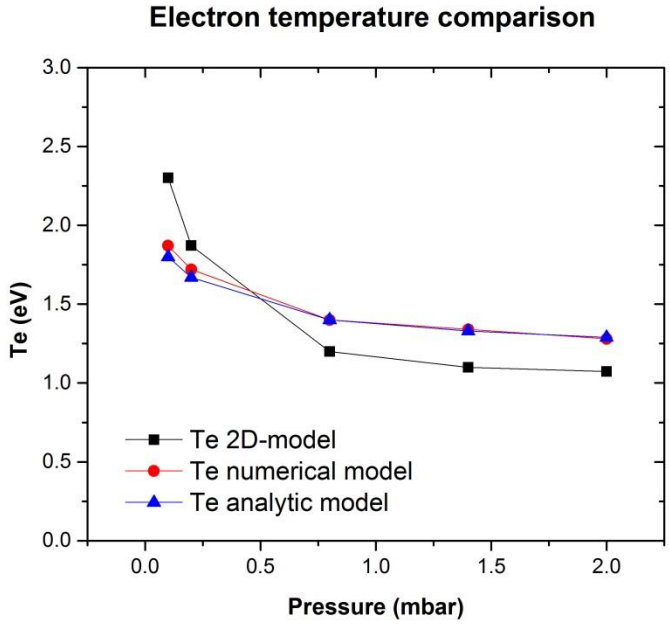

Figure 10. The electron temperature of the different models as function of pressure.

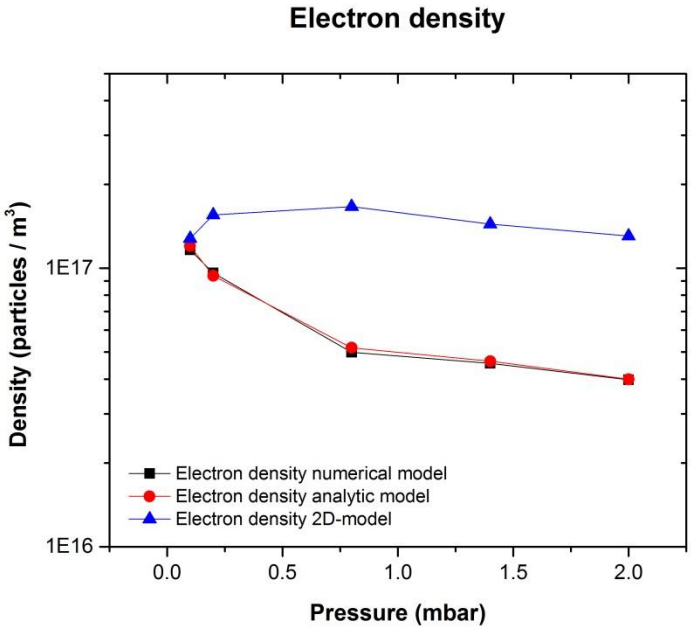

Figure 11. The electron density of the different models as function of pressure. The values are in the same order of magnitude, but the trend is different for pressures below 0.8 mbar.

The densities of the other species are found in the next five figures. The densities of H_2^+ and H^+ of the analytic and global model are in agreement and show similar trends as the 2D-model. However the absolute values of the densities of the 2D-models are up to a factor 12 higher for 0.1 mbar. The decreasing densities can be understood by regarding the earlier mentioned decrease in electron temperature with pressure. It is this strong effect that causes less effective ionization and lower ion densities at higher pressures despite increasing collision frequencies.

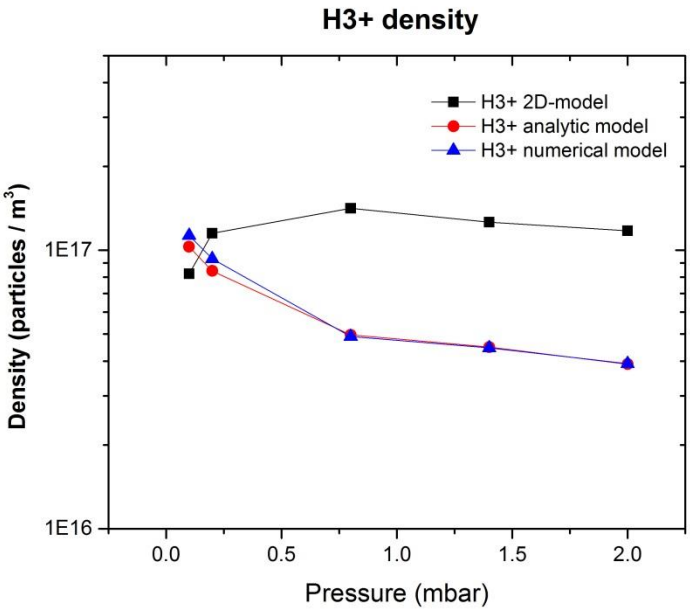

Figure 12. The H_3^+ density of the different models as function of pressure. The absolute density values of the three models are in the same order of magnitude. The trends of the models is however different for 0.1 and 0.2 mbar. The reason for this is the deflected trend of the electron temperature.

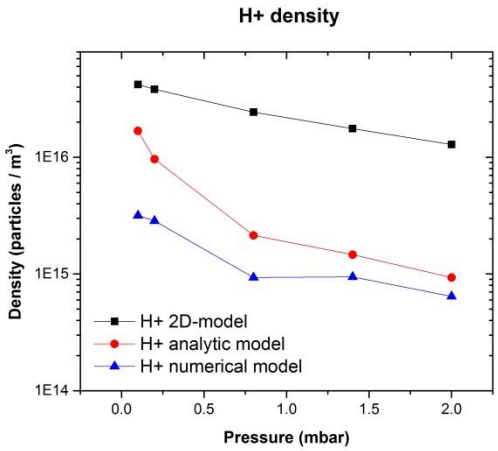

Figure 13.1 The H^+ density of the different models as function of pressure. The three models show equal trends. The value of 0.8 mbar shows for both global models a slight deviation from the 2D trend.

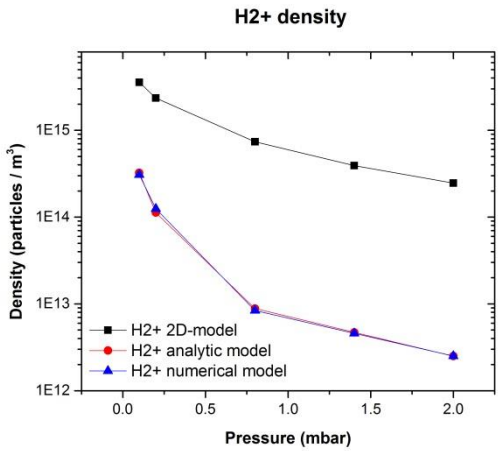

Figure 13.2 The H_2^+ density. Trends are similar and the global models are in very good agreement. The absolute values of the 2D-model compared to the two global models show however a large difference up to a factor 100.

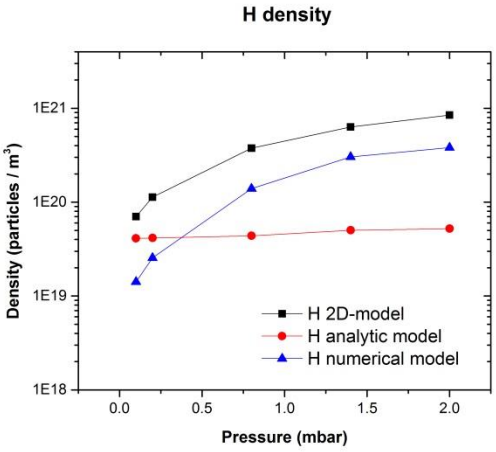

Figure 14.1 The H density of the different models as function of pressure. The analytic model shows a straight line instead of a curve like the numerical and 2D-model.

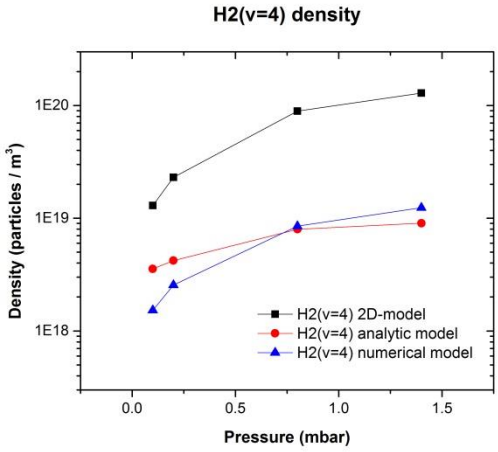

Figure 14.2 The $H_2^{v=4}$ density of the different models as function of pressure. The three models show similar trends

Concerning the vibrational excited hydrogen, all models are in agreement. The increasing numbers of vibrational excited hydrogen can be explained with the increasing electron collision frequency at higher pressures and a lower diffusion loses at the walls. The lower electron temperature has less influence on this reaction than on the ionization reaction since the disociation energy of hydrogen is much smaller than the ionization energy. Remarkable are the deviations of the analytic model form the other two models for the density of atomic hydrogen. According to the analytic model the hydrogen density stays approximatly the same, while the other models show an increase. The recombination rate of the the deexciation of excited hydrogen is similar to the of atomic hydrogen and this rate gives a right trend. The cause of the strange behaviour of atomic hydrogen has therfore probabliy to do with the averaging method for the hydrogen recombination probability.

An overview of the three models is given in table 7. In this table the densities and electron temperature are given as fraction of the density and electron temperature in the 2D-model.

Analytic and numerical model compared to the 2D-model at 0.8 mbar

Species	Analytic model	Numerical model
H_2	1.067	1.063
H	0.117	0.371
e	0.311	0.300
$H_2^{v=4}$	0.112	0.093
H^+	0.088	0.038
H_2^+	0.012	0.011
H_3^+	0.351	0.346
T_e	1.167	1.167

Table 7. Density of all species as fractions of the average density in the 2D-model. This table gives an overview of the differences between the models. The largest deviation is a factor 0.011 for the H_2^+ density. For both models the amount of H_2 is too high and the amount of other species too low. This may indicate a shortage of energy in the plasma due to a too large energy loss at the walls.

The pressure of the plasma in PLASIMO can be regulated by changing the initial densities of the species. Using the ideal gas law one can choose a pressure and temperature and calculate the number of initial particles. However, since molecular hydrogen can be split into two hydrogen atoms, the number of particles in the plasma changes during the simulation. Consequently the final pressure shows a deviation from the initial pressure by a few percent.

2.3.4. Results of modelling only the inner part of the volume

The plasma is mainly positioned around the quartz tube, see figure 15. In order to obtain a better description of the plasma, only the inner 4.5% of the total volume is modeled and compared with the average values of the 2D-model is this region. The reasons for modelling this percentage of the volume is the fact that for the associated radius of this volume (r=24 mm), the ion densities dropped to approximately 5% of the maximum value, indicating the start of the less reactive part of the plasma. Since the ions show a strong peaked distribution around the inner quartz tube (see figure 4), we expect their densities to show more similarities with the 2D-model. Table 8 shows that this is indeed the case. $H_2^{v=4}$ and *H* have no strong peak in their distribution (see figure 15). As a consequence no major improvements take place, only a small improvement for H and a slight deterioration for $H_2^{v=4}$. In general, the results of this approach show significant improvements as is shown by table 8. We also tried a smaller volume of 0.8% with an associated radius of 17mm (the radius at which the density at the inner wall is reached again). This volume shows improvements for H, H^+, H_2^+ , however the other densities are deteriorating. A larger part of the volume is also modeled. The associated radius of this volume is chosen to be half of the maximum radius (45mm), leading to a volume equal to 23% of the total volume. This volume shows improvement relative to the total volume approach, but the results are not improvement relative to the smaller volume of 4.5%.

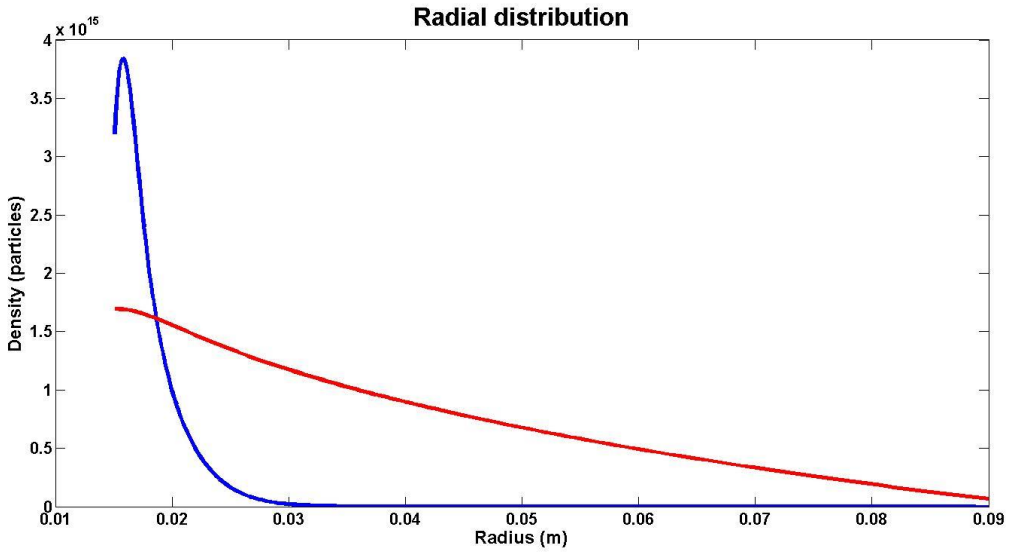

Figure 15. The radial distribution of the H_2^+ ion of the 2D-model is depicted in blue and the density of H is depicted with the red line (the density of H is multiplied with 10^{-6} for illustrative purpose). The density of H_2^+ density is peaked near the inner quartz tube and therefore shows that the plasma is mainly positioned around the center of the coaxial vessel. H show a distribution that is not peaked and therefore no improvements are found for this species when modelling only the inner volume.

Numerical model of the total volume and inner volume compared at 0.8 mbar

Species	Numerical model Total volume	Numerical model Inner 0.8% of the volume	Numerical model Inner 4.5% of the volume	Numerical model Inner 23% of the volume
H_2	1.06	1.06	1.09	1.09
H	0.38	0.49	0.44	0.39
e	0.30	3.88	0.95	0.55
$H_2^{v=4}$	0.10	0.08	0.09	0.09
H^+	0.04	0.28	0.15	0.08
H_2^+	0.01	0.62	0.13	0.05
H_3^+	0.35	5.63	1.22	0.65
T_e	1.17	0.79	0.97	1.16

Table 8. Density of all species as fractions of the average density in the 2D-model. For the comparison of the global model with the 2D-model for the inner 4.5% of the volume, the value of the global model is compared with the average density of the 2D-model for the inner 4.5% of the volume. Modeling the inner 4.5% of the volume does result in better results. Other pressures show equal results.

2.3.5 Comparison of the 2D-model with experiments

In the previous section the 2D-model is used to benchmark the two global models. The validity of the 2D-model itself will be discussed in this section. In the thesis of S. Rahimi, the model is compared with experimental results obtained with optical emission spectroscopy. These results are displayed in figure 16 and 17. In figure 16 the electron temperature is plotted against the axial position. The radial position is 1 mm from the quartz tube. In figure 17 the electron density can be found as function of the axial coordinate. The radial position is also 1 mm from the quartz wall. The values of the electron density are in the same order of magnitude. For the electron temperature, there is a rather large deviation for 0.1 mbar, the modeled value is nearly two times too high. However, in general the experimental results show good agreement with the experiments and subsequently the 2D-model can be considered as a good benchmark for the global models.

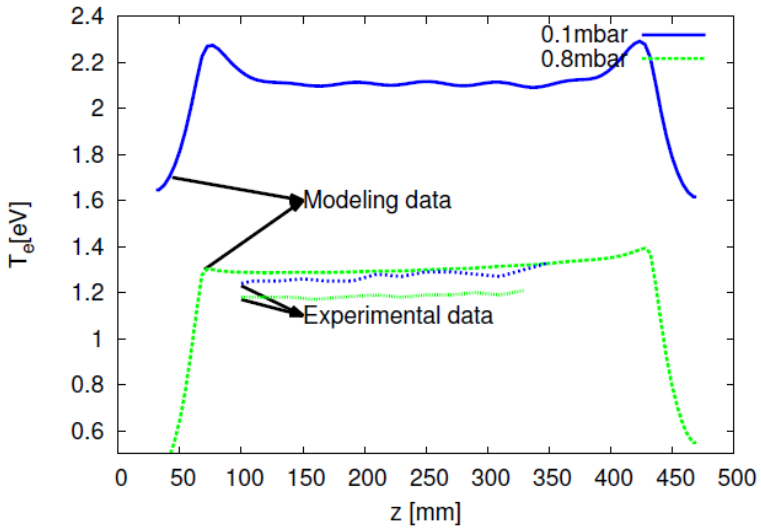

Figure 16.The electron temperature is plotted against the axial position. The radial position is 1 mm from the quartz tube [1].

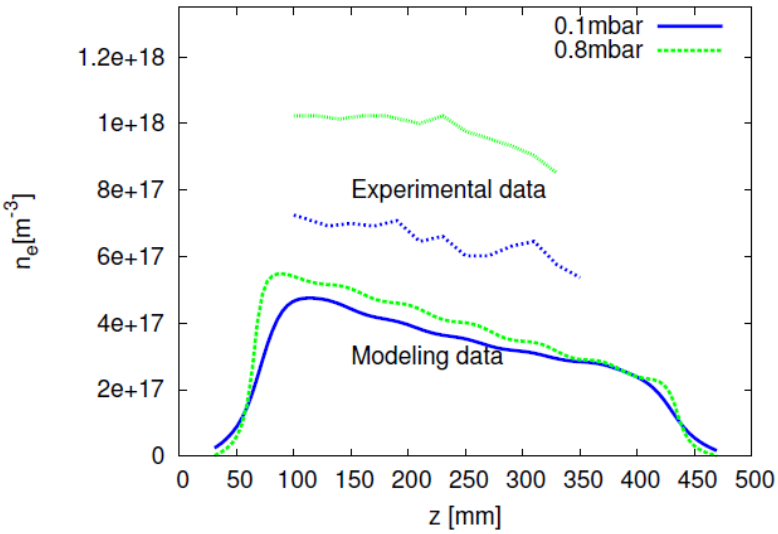

Figure 17. The electron density against the axial position. The radial position is 1 mm from the quartz tube [1].

2.4 Conclusion

Two different global models are created and compared the 2D-model of S. Rahimi. The first global model, referred to as the analytic model, made use of analytic expressions to calculate the reaction rates of the plasma wall reactions. The second global model, referred to as the numerical model, made use of the densities at the walls gained from the 2D-model to obtain the reaction rates for the wall reactions. Both models are compared with the 2D-model. The latter is a good choice as benchmark since its results are supported by experimental results. It was found that the two global models are in good agreement and in reasonable agreement with the 2D-model. The H_3^+ density of the two global models shows an opposite trend for pressure lower than 0.8 mbar. This is a result of the deviation of the electron temperature at these pressures. Since H_3^+ is the majority ion and quasi neutrality is used to obtain the electron density, the electron density shows similar behavior. A second important disagreement is the H^+ density of the analytic model, which does barely increase with pressure. A reason for this is probably the averaging method for the recombination probability. In an attempt to get a better agreement with the 2D-model, a model was made considering only the area around the inner quartz tube. This model showed however some significant improvements. For further research one could take a more profound look at the transport of the global model, since there are some large differences between the transports obtain from the 2D-model and those obtain from literature. More insight in transport may lead to a better understanding of the differences between the models and to better results. Something else that deserves attention in further research is the assumption that all species are perfectly mixed. The distributions of the species from the 2D-model show however different distribution, indicating that the species are not perfectly mixed at all. The same applies for the electron temperature. Since many reaction rates depend on the electron temperature, the reaction rates also have a spatial distributions. It might be interesting to average these distributions and compare them with the average rates of the global model, which are obtained with an average electron temperature. Since the dependency of the rates is nonlinear (mainly exponential), the average reaction rates of the 2D-model are likely to show significant difference from those of the global model. For understanding the differences between both models, the magnitude of the differences in rate coefficients is of course of great interest.

3 Zero-dimensional Hydrogen-Silane model

3.1 Introduction

Plasmas can be used to deposited thin layers of material on surfaces. One of the techniques that make use of this principle is plasma enhanced chemical vapor deposition (PECVD). This method is typical used to deposit thin amorphous silicon films on solar cells. For the production of solar cells it is interesting to have a model that describes this deposition plasma. The aim of this section is therefore to create a time-dependent zero-dimensional model of a hydrogen-silane plasma discharge in a coaxial microwave. The model is based on a two-dimensional model of this coaxial microwave made by S. Rahimi [1]. The geometry and input power of the system are the same as for the hydrogen plasma of chapter 2 and the modeling is done in PLASIMO once again.

3.2 Model

3.2.1 Species and volume reactions

In the hydrogen-silane plasma, hydrogen and silane are the two background gases. Electrons cause dissociation of both hydrogen and silane leading to the formation of H, SiH_3, SiH_2 and Si_2H_5. The latter three silane molecules are responsible for the deposition. Besides the formation of neutrals a lot of different ions are created: H^+, H_2^+, H_3^+, SiH_3^+, SiH_3^- and SiH_2^+. An overview of the reactions in which these species are created can be found in table 10.

3.2.2 Wall reactions

The wall reactions in the hydrogen-silane plasma are very similar to the wall reactions in the hydrogen plasma. There is also ion neutralization, recombination and vibrational de-excitation. Besides these reactions an extra type of wall reaction takes place: the deposition of SiH_3, SiH_2 and Si_2H_5 on the walls. The deposition rate is described with a sticking coefficient. Literature gives sticking coefficients of 0.09, 0.8 and 0.09 respectively [17]. This sticking process can be modeled by implemented one way reactions like: $SiH_3 \rightarrow SiH_{3_{sticking}}$. The consequence of modeling like this is a constant loss of SiH_3 since $SiH_{3_{sticking}}$ can not be returned to SiH_3 or any other particle to join the plasma. Without an inflow of silane the deposition reaction will stop. The latter is very difficult to realize in Plasimo, this is therefore probably the reasons why Rahimi did not model the sticking process. She considered the sticking coefficient as a recombination probability. The particles SiH_3, SiH_2 and Si_2H_5 do not stick to the walls, but recombine with hydrogen to SiH_4. This process results in an additional flux of silane into the plasma, but since there is already a large amount of silane present this flux has only a small influence on the plasma composition, according to Rahimi.

The sticking reactions are found as reactions 9, 10 and 11 in table 9. Despite the sticking not being modeled, the deposition rate can still be obtained from the reaction rates of these sticking reactions.

Some of the SiH_2 and Si_2H_5 molecules that collide with the wall can recombine with hydrogen to form silane. This process is described with a wall recombination probability. For SiH_2 and Si_2H_5 a recombination probability of 0.17 is used [18]. The reaction rates for the neutral and ion wall-reactions are similar to those of the hydrogen model. The rate coefficients of the wall recombination are however slightly different. In the hydrogen model the following wall recombination takes place: $H + H \rightarrow H_2$. The rate of this reaction is described with the flux of hydrogen to the walls:

$$\mathrm{R}_{\mathrm{recombination}} = \gamma_H \, \Gamma_H = \gamma_H \, \frac{D_{eff}}{\Lambda^2} n_H, \tag{14}$$

with γ_H the recombination probability, Λ the diffusion length and D_{eff} the effective diffusion coefficient of hydrogen. In the hydrogen-silane plasma however, not one type of species recombines, but two. The wall reactions $SiH_3 + H \rightarrow SiH_4$ includes SiH_3 and H. In this case it is not obvious what to use for the diffusion coefficient. Here is decided to use the smallest diffusion coefficient (the of SiH_3), since this coefficient is the bottle neck of the reaction. The same is done for the other wall recombination: $Si_2H_5 + 3H \rightarrow 2\,SiH_4$. Here the diffusion coefficient of Si_2H_5 is used. Both coefficients are calculated with use of the Einstein-Smoluchowski equation :

$$D = \frac{\lambda^2}{2\tau}, \tag{24}$$

with D the diffusion coefficient, λ the mean free path and τ the average time between collisions. The latter can be expressed as function of the mean free path and average thermal velocity v_{av}:

$$\tau = \frac{\lambda}{v_{av}}, \tag{25}$$

with v_{av} equal to

$$v_{av} = v_{th} = \sqrt{\frac{8k_BT}{\pi m}}. \tag{26}$$

In this equation k_B is the Boltzmann constant, T the temperature and m the mass of the molecule. Substituting (25) in (24) gives us

$$D = \frac{1}{2}\lambda v_{av}\,. \tag{27}$$

The mean free path is defined as

$$\lambda = \frac{RT}{\sqrt{2}\pi d^2 N_A P}, \tag{28}$$

where R is the gas constant , T the temperature, N_A the number of Avogadro, P the pressure and *d* the average diameter of the background species and the species for which the mean free path is calculated [18]. The reasons for using this equation is that it makes use of the hard sphere radii of the species and these are already provided by S. Rahimi. All wall reactions can be found in table 9.

#	Reaction	Reaction rate
1	$H \rightarrow \frac{1}{2} H_2$	$\mathrm{R}_{Recombintion} = \gamma_H \frac{D_{eff}}{\Lambda^2} n_H$
2	$H_2^{v=4} \rightarrow H_2$	$\mathrm{R}_{\mathrm{de-excitation}} = \frac{D_{eff}}{\Lambda^2} n_{H_2^{v=4}}$
3	$H^+ \rightarrow H$	$R_{neutralization} = v_B(2\pi R^2 n_{sL} + 2\pi R L n_{sR})$
4	$H_2^+ \rightarrow H_2$	$R_{neutralization} = v_B(2\pi R^2 n_{sL} + 2\pi R L n_{sR})$
5	$H_3^+ \rightarrow H + H_2$	$R_{neutralization} = v_B(2\pi R^2 n_{sL} + 2\pi R L n_{sR})$
6	$SiH_3^+ \rightarrow SiH_3$	$R_{neutralization} = v_B(2\pi R^2 n_{sL} + 2\pi R L n_{sR})$
7	$SiH_2^+ \rightarrow SiH_2$	$R_{neutralization} = v_B(2\pi R^2 n_{sL} + 2\pi R L n_{sR})$
8	$SiH_3^- \rightarrow SiH_3 + e$	$R_{neutralization} = v_B(2\pi R^2 n_{sL} + 2\pi R L n_{sR})$
9	$SiH_3 + H \rightarrow SiH_4$	$\mathrm{R}_{sticking} = s_{SiH_3} \frac{D_{eff}}{\Lambda^2} n_{SiH_3}$
10	$SiH_2 + H_2 \rightarrow SiH_4$	$\mathrm{R}_{sticking} = s_{SiH_2} \frac{D_{eff}}{\Lambda^2} n_{SiH_2}$
11	$Si_2H_5 + 3H \rightarrow 2\,SiH_4$	$\mathrm{R}_{sticking} = 2\, s_{Si_2H_5} \frac{D_{eff}}{\Lambda^2} n_{Si_2H_5}$
12	$Si_2H_5 + 3H \rightarrow 2\,SiH_4$	$\mathrm{R}_{Recombintion} = 2\, \gamma_{Si_2H_5} \frac{D_{eff}}{\Lambda^2} n_{SiH_5}$
13	$SiH_3 + H \rightarrow SiH_4$	$\mathrm{R}_{Recombintion} = \gamma_{SiH_3} \frac{D_{eff}}{\Lambda^2} n_{SiH_3}$

Table 9. Overview of the wall reactions. In the report of S.Rahimi reaction 12 is mention as the recombination of Si_2H_5 with recombination probability 0.17. The reaction is however not fully written out in the report neither it can be found in the model. Here we made the assumption that Si_2H_5 recombines similar to SiH_3, so it recombines with three hydrogen atoms to form silane. The rate coefficient of reaction 12 is multiplied by two, because for each Si_2H_5 that recombines at the wall, two silane molecules are formed. The same applies for reaction 11.

#	Reaction	Reaction rate coefficient $K_r(T)$	Ref.
1	$H_2 + e \leftrightarrow H_2^+ + 2e$	$1.58 \cdot 10^{-14}\, T_e^{0.5} e^{-\frac{15.378}{T_e}}$	[6]
2	$H_2 + e \leftrightarrow 2H + e$	$1.413 \cdot 10^{-15}\, T_e^{2} e^{-\frac{4.48}{T_e}}$	[6]
3	$H + e \rightarrow H^+ + 2e$	$1.914 \cdot 10^{-14}\, T_e^{0.758} e^{-\frac{9.56}{T_e}}$	[6]
4	$H_2^+ + e \rightarrow H^+ + H + e$	$6.8 \cdot 10^{-15} T_e^{1.571} e^{-\frac{2.7}{T_e}}$	[6]
5	$H_3^+ + e \rightarrow H_2 + H$	$9.7 \cdot 10^{-14} T_e^{-0.5}$	[7]
6	$H_2^+ + e \rightarrow 2H$	$5.66 \cdot 10^{-14} T_e^{-0.5}$	[7]
7	$H^+ + e \rightarrow H$	$2.62 \cdot 10^{-19} T_e^{-0.5}$	[7]
8	$H_2^+ + H_2 \rightarrow H_3^+ + H$	$2.1 \cdot 10^{-15}$	[8]
9	$H_2 + H \leftrightarrow 3H$	$5.6 \cdot 10^{-15} T_{H_2}^{0.419} e^{-\frac{4.478}{T_{H_2}}}$	[8]
10	$2H_2 \leftrightarrow 2H + H_2$	$5.6 \cdot 10^{-15} T_{H_2}^{0.419} e^{-\frac{4.478}{T_{H_2}}}$	[8]
11	$H_2 + e \leftrightarrow H_2^{v=4} + e$	$4.69 \cdot 10^{-16} T_{H_2}^{0.8202} e^{-\frac{1.89}{T_{H_2}}}$	[8]
12	$H_2^{v=4} + H^+ \rightarrow H_2^+ + H$	$2.5 \cdot 10^{-15}$	[8]
13	$SiH_4 + e \rightarrow SiH_3 + H + e$	$7.7 \cdot 10^{-14} T_e^{0.5} e^{-\frac{10.6}{T_e}}$	[10]
14	$SiH_4 + e \rightarrow SiH_2 + H_2 + e$	$1.6 \cdot 10^{-13} T_e^{-1} e^{-\frac{10.6}{T_e}}$	[10]
15	$SiH_4 + e \rightarrow SiH_3^+ + H + 2e$	$1.6 \cdot 10^{-13} T_e^{-1}.3 e^{-\frac{15.9}{T_e}}$	[10]
16	$SiH_4 + e \rightarrow SiH_2^+ + H_2 + 2e$	$3.56 \cdot 10^{-13} T_e^{-1.2} e^{-\frac{15.5}{T_e}}$	[10]
17	$SiH_4 + e \rightarrow SiH_3^- + H$ *Note	$2.5 \cdot 10^{-13}$	[7]
18	$Si_2H_6 + e \rightarrow SiH_3 + SiH_2 + H + e$	$3.72 \cdot 10^{-10}$	[7]
19	$SiH_2^+ + e \rightarrow SiH_2$	$1.13 \cdot 10^{-13}$	[9]
20	$SiH_3^+ + e \rightarrow SiH_2 + H$	$1.69 \cdot 10^{-13}$	[9]
21	$SiH_4 + H \rightarrow H_2 + SiH_3$	$2.8 \cdot 10^{-17} e^{-\frac{1250}{T_h}}$	[9]
22	$Si_2H_6 + H \rightarrow Si_2H_5 + H_2$	$1.6 \cdot 10^{-16} e^{-\frac{1250}{T_h}}$	[9]
23	$Si_2H_6 + H \rightarrow SiH_3 + SiH_4$	$0.8 \cdot 10^{-16} e^{-\frac{1250}{T_h}}$	[9]
24	$H_2 + SiH_2 \rightarrow SiH_4$	$3 \cdot 10^{-18}(1 - (1 + 2.3 \cdot 10^{-2} p_0)^{-1})$	[9]
25	$SiH_3 + H \rightarrow SiH_2 + H_2$	$5 \cdot 10^{-16}$	[12]
26	$SiH_3 + SiH_3 \rightarrow SiH_4 + SiH_2$	$1 \cdot 10^{-17}$	[9]
27	$SiH_4 + SiH_2 \rightarrow Si_2H_6$	$2.0 \cdot 10^{16}(1 - (1 + 0.33 p_0)^{-1})$	[9]
28	$Si_2H_6 + SiH_2 \rightarrow Si_3H_8$	$4.2 \cdot 10^{16}(1 - (1 + 0.32 p_0)^{-1})$	[9]
29	$2Si_2H_5 \rightarrow Si_3H_8 + SiH_2$	$1.5 \cdot 10^{-16}$	[9]
30	$Si_3H_8 + H \rightarrow Si_2H_5 + SiH_4$	$2.4 \cdot 10^{-17} e^{-\frac{1250}{T_h}}$	[9]
31	$SiH_2^+ + SiH_4 \rightarrow SiH_3^+ + SiH_3$	$1.1 \cdot 10^{-15}$	[13]
32	$SiH_2^+ + H_2 \rightarrow SiH_3^+ + H$	$1.1 \cdot 10^{-15}$	[13]
33	$SiH_4 + H_3^+ \rightarrow SiH_3^+ + 2H_2$	$5.16 \cdot 10^{-16}$	[13]
34	$SiH_4 + H_2^+ \rightarrow SiH_3^+ + H + H_2$	$6.2 \cdot 10^{-16}$	[13]
35	$SiH_4 + H^+ \rightarrow SiH_3^+ + H_2$	$5 \cdot 10^{-16}$	[13]
36	$SiH_3^+ + SiH_3^- \rightarrow 2SiH_3^+$	$7.22 \cdot 10^{-12} \left(\frac{T_h}{300}\right)^{-0.5}$	[9]
37	$SiH_3^- + SiH_2^+ \rightarrow SiH_3 + SiH_2$	$7.1 \cdot 10^{-12} \left(\frac{T_h}{300}\right)^{-0.5}$	[9]
38	$H_3^+ + SiH_3^- \rightarrow H_2 + SiH_4$	$1.27 \cdot 10^{-12} \left(\frac{T_h}{300}\right)^{-0.5}$	[9]
39	$H_2^+ + SiH_3^- \rightarrow H_2 + SiH_3$	$8.76 \cdot 10^{-13} \left(\frac{T_h}{300}\right)^{-0.5}$	[9]
40	$H^+ + SiH_3^- \rightarrow SiH_4$	$4.51 \cdot 10^{-13} \left(\frac{T_h}{300}\right)^{-0.5}$	[9]

Table 10. Overview of the volume reactions.

Note: Reaction 17 is in the report of S.Rahimi written as $SiH_4 + e \rightarrow SiH_3^- + 2e$, which does not satisfy conservation of charge. In her model file and in the reference the reaction is however written as $SiH_4 + e \rightarrow SiH_3^- + H$. This latter is also the reaction used here.

3.3 Results and discussion

3.3.1 Comparison between the global model and the 2D-model

In this section the results of the global model are presented and discussed. In chapter 2 a detailed comparison is made between the global model and the 2D-model. Unfortunately we were not able to make the 2D-model of the hydrogen silane plasma work. As a consequence we have no raw data of the 2D hydrogen silane model. We made however still a comparison between the two models using the figures and the description of the thesis.

The electron properties of the electrons are depicted in the following two figures. The electron temperature can be seen in figure 19. Although the magnitude of the temperature is comparable to the temperatures of the 2D-model, the trend is the opposite: an increase with pressure instead of a decrease. The total temperature gain is only 0.1 eV, which is not a large increase. A possible explanation for this opposite behavior can be a faulty estimation of the absorbed power, however adapting the input power yields no change of the trend. Another reason could be the decrease in electron density with pressure (see figure 18). Since the input power is absorbed by the electrons, less electrons result in a higher absorbed power per electron. As a consequence the electrons temperature rises. The major loss of electrons is caused by reaction 17, the formation of SiH_3^- from silane. The production of electrons is mainly determined by the ionization of atomic hydrogen. Referring to figure 14.1 of section 2.3.3, one can see the deviation of the trend of atomic hydrogen for the analytic model compared to the 2D model. Without the results of the 2D silane model, we were forced to use the same analytic expression for the hydrogen wall recombination. The latter could result in a density for atomic hydrogen that is too low for higher pressures and as a consequence the electron production starts lacking behind. Due to this lower production the electron density is falling too fast, resulting in a higher electron temperature.

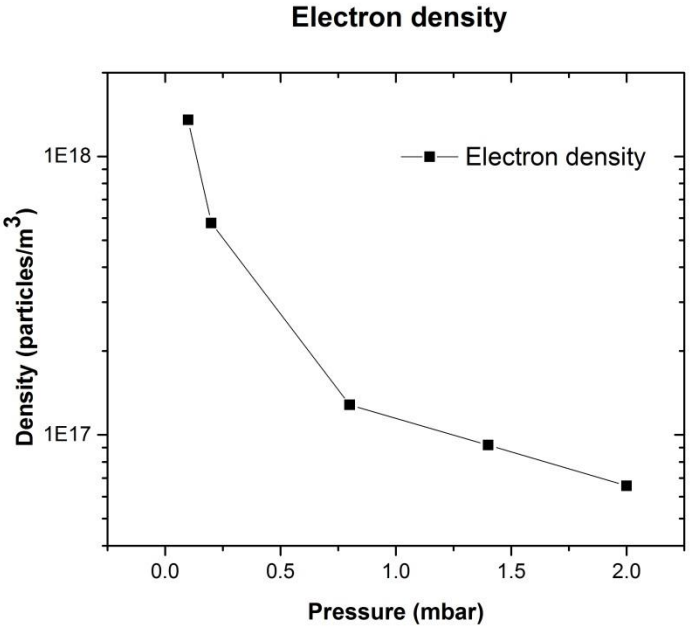

Figure 18. The electron density as function of pressure. The electron density is decreasing with increasing pressure.

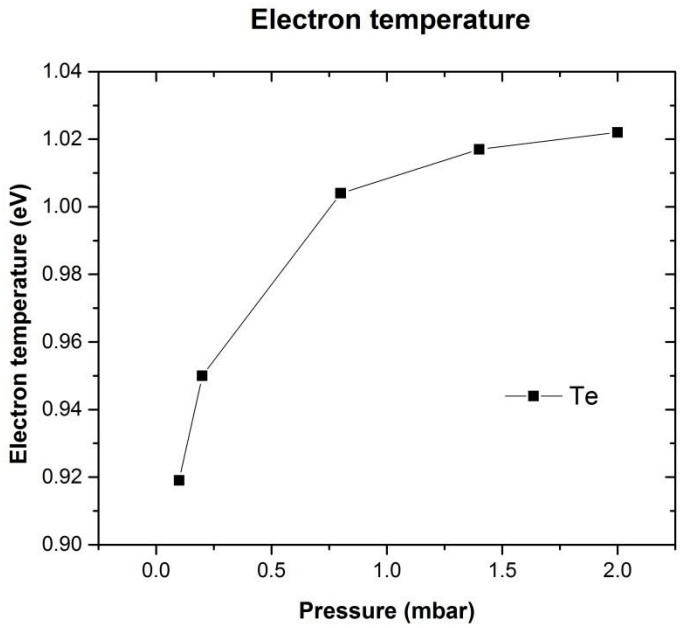

Figure 19. The electron temperature as function of pressure. The electron temperature is increasing as function of pressure, the opposite of the 2d-model. Possible explanation for this is an electron density that is falling too fast with increasing pressure. This is resulting in a smaller group of electrons absorbing the same input power. As a consequence the electron temperature is increasing.

The deposition rate is decreasing with increasing pressure. This was also found with the 2D model of Rahimi and by experiments [16]. The reasons for a smaller deposition rate, is a smaller flux of the radicals to the walls. The flux to the walls decreases due to a smaller mean free path and so a smaller diffusion.

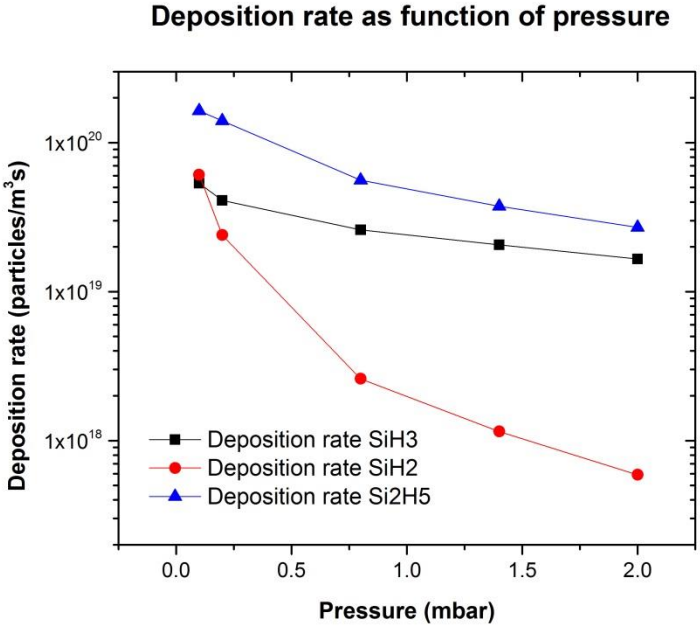

Figure 20. The deposition rates of the different silane radicals as function of pressure. The rate is given in particles/m^3s: the amount of particles deposited per second per m^3 of plasma. The total deposition rate is obtained by multiplying with the total plasma volume. With increasing pressure the deposition rates drop. This is probably caused by a lower diffusion of these radicals to the walls.

The radicals SiH_3, SiH_2 and Si_2H_5 are important for their role in silicium deposition. The behavior of their densities is therefore investigated as function of pressure. It is found that the densities of SiH_3 and Si_2H_5 increase with pressure. This is probably due to smaller diffusion loses at the walls. The mean free path will decrease with increase of pressure, see eq. 27. The density of SiH_2 is falling with increase of pressure, despite the smaller diffusion losses. This is a result of the destruction reactions 24, 27 and 28 of table 10. These rates are increasing with increasing pressure causing a larger destruction that can't be compensated by smaller diffusion losses. The most prominent radical is found to be Si_2H_5, just like in the 2D-model. At low pressures (< 0.8 mbar), Rahimi found SiH_3 to have the smallest density and for higher pressures (> 0.8 mbar) SiH_2 has the smallest density. In the global model SiH_3 has the smallest density for pressures lower than 0.2 mbar. Above this pressure, SiH_2 has the smallest density.

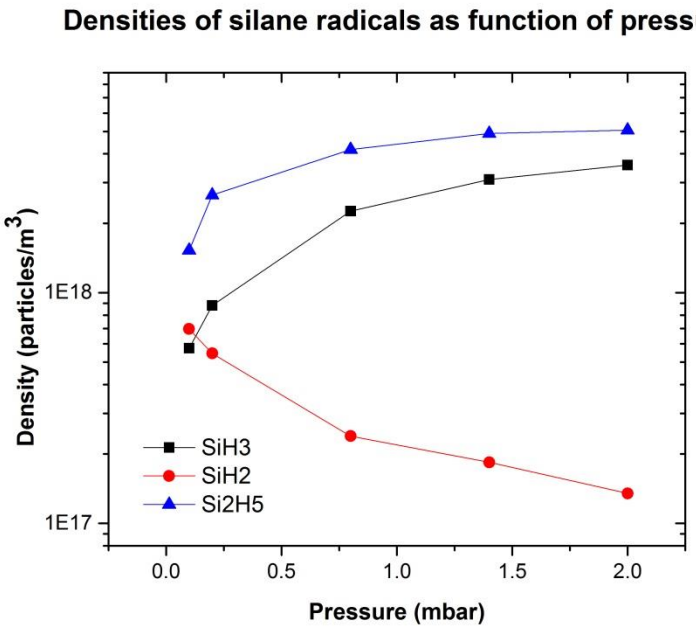

Figure 21. Densities of the radicals: SiH_3, SiH_2 and Si_2H_5 as function of pressure. The densities of SiH_3 and Si_2H_5 are increasing in with increasing pressure, caused by the smaller diffusion losses at the walls. The density of SiH_2 is falling with increase of pressure, despite the smaller diffusion losses. This is a result of the destruction reactions 24, 27 and 28 of table 10. These rates are increasing with increasing pressure causing a larger destruction that can't be compensated by smaller diffusion losses.

In the model of S.Rahimi the temperature of the heavy particles is a variable, in the global model, this value is constant. Unlike with the 2D hydrogen model, the 2D silane didn't work. Therefore no data are available of the heavy particle temperature. In the global silane model the same value as for the hydrogen model is used: 500 K. Figure 5.4 in the thesis of Rahimi however, suggest a higher temperature. According to the ideal gas law, a higher temperature implements fewer particles for the same pressure. Besides this some reactions depend specifically on the heavy particle temperature. The differences caused by a possible faulty heavy particle temperature should be kept in mind.

3.3.2 Influence of the hydrogen recombination probability on the deposition rate

In chapter two it is already told that literature is ambiguous about the value of the wall recombination probability of hydrogen. It has however a major influence on the hydrogen density and might also influence the reactions involved in the creation of radicals. In section 2.3.2 it was found that the contribution of the quartz recombination value is negligible compared to the value of the metal recombination probability. Based on this observation we only varied the steel wall recombination probability. The value is changed from 0 to 0.2 (the maximum value reported by literature [1]) at a pressure of 0.8 mbar and an input power of 1500 W. Figure 22 shows the effect of changing the wall recombination probability. Surprisingly, the effect seems to be negligible. Nearly no change is observed. According to the global model less than 10 percent of the hydrogen is lost by wall recombination. Most of the hydrogen disappears in the reactions $SiH_3 + H \rightarrow SiH_2 + H_2$ and $SiH_4 + H \rightarrow H_2 + SiH_3$. This explains the small effect of the probability value. In the 2D-model of Sara Rahimi however an increase is observed for a lower recombination probability. A decrease of the steel wall recombination probability from 0.1 to 0.004 leads to estimated depositions of SiH_3, SiH_2 and Si_2H_5 that are respectively 4.9, 5.2 and 1.8 times larger.

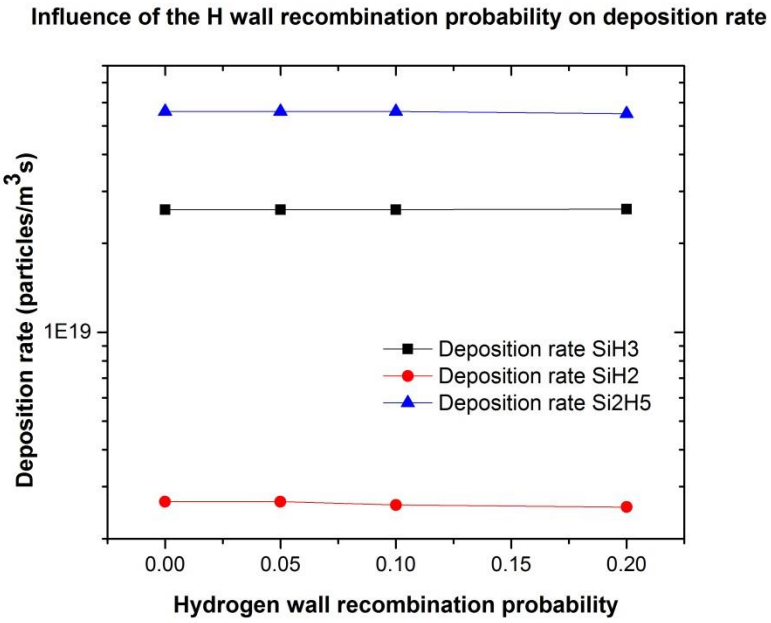

Figure 22.The effect of the hydrogen wall recombination probability on the deposition rate. The steel wall probability is varied from 0 to 0.2 at a pressure of 0.8 mbar and a input power of 1500 W.

3.3.3 Influence of the input power on the deposition rate

The effect of the input power on the deposition rate is shown in the figure below. As one can see, an increase of input power leads to a higher deposition rate of all species. The same result was found by Rahimi. A higher input power results in more electrons (see fig. 20), leading to a higher electron-neutral collision frequency. The latter increases the production of radicals and hence a higher deposition rate.

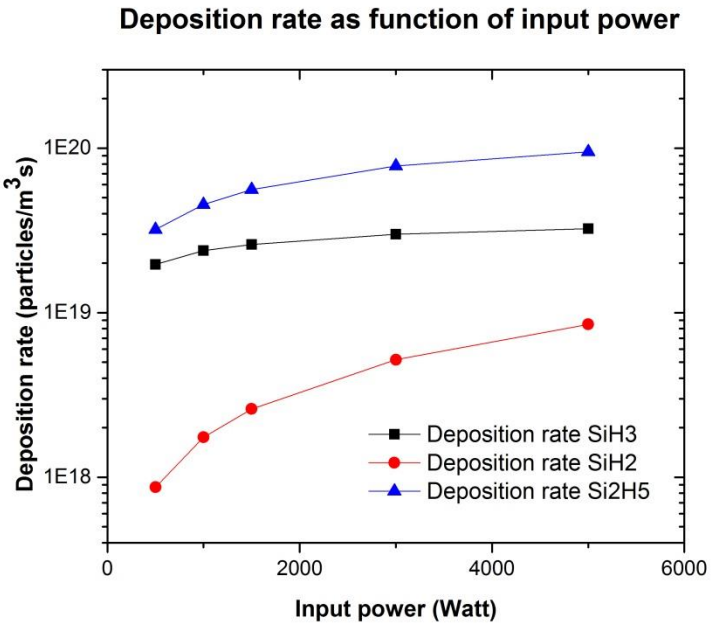

Figure 23. The effect on input power on the deposition rate. The pressure is 0.8 mbar.

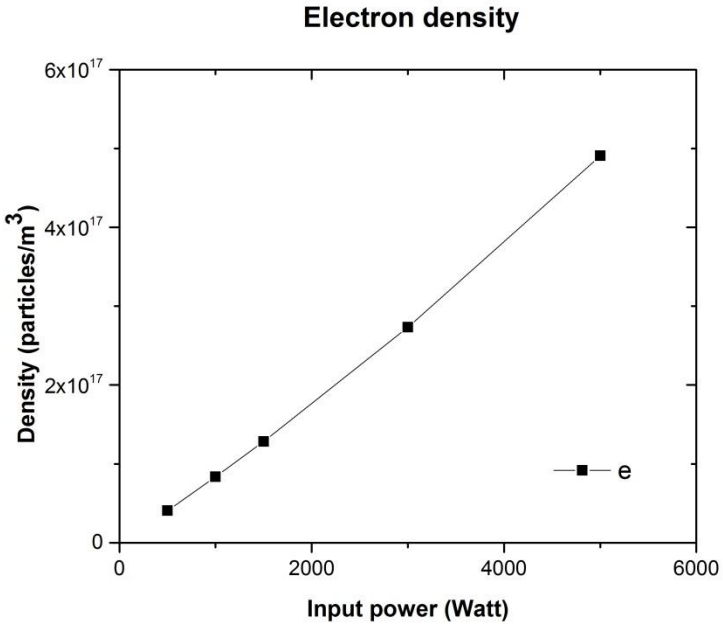

Figure 24. Electron density as function of the input power. Increase of input power leads to a nearly linear increase in electron density. The latter will cause a larger production of radicals leading to a higher deposition rate.

3.4 conclusion

The global hydrogen-silane model showed several similarities with the 2D-model of S. Rahimi. Both models agree on the important fact that deposition rates fall when pressure increases. This result is backed up with experimental results. Furthermore it is found that the deposition rate increases with increase of power. No significant effect was observed when the hydrogen wall recombination was changed. The order of magnitude for the densities of the silane radicals is the same in both models. For a next deposition model, it would be interesting to model the sticking process with the use of a silane inflow, rather than treating the deposition process as recombination reaction. This may lead to different results since a silane inflow will introduce a new variable that influence the plasma properties and the deposition rate. A large inflow can for example lead to a higher silane-hydrogen ratio influencing reaction rates. Different results are expected and therefore worthwhile to investigate.

Extension final Bachelor project

4 Pulsed power input

4.1 Introduction

Plasma enhanced chemical vapor deposition (PECVD) is a well-known method to deposit layers of materials on surfaces. The technique uses constant power plasma for the deposition. In order to control the deposition process, there are a few parameters that can be changed. One of the parameters is pressure. In the previous chapter it is for example shown that a higher pressures leads to a lower deposition rate. Another parameter is the amount of power that is supplied to the plasma. Higher power input leads often to more radicals and therefore to a more reactive plasma. For silane plasma it results therefore in a higher deposition rate. Besides the magnitude of power, the time dependency of the power can be changed. The power can be pulsed for example. During a pulse the electron temperature rises and leads to an exponential increase of the reaction rates (see reaction rates in table 10 of chapter 2). Also contributing to higher reaction rates is the even higher electron temperature during the peak at the beginning of the pulse, this peak can be as high as 8 eV and result in very large reaction rates, although this is for a very short time. The cause of this peak is a strongly reduced electron density. All input power is therefore absorbed by only a few remaining electrons. The temperature of these electrons will consequently rise to great height. As a result of this, the reaction rates increase and lead to a large amount of radicals that can contribute to deposition. Pulsing could be very interesting if the higher deposition during pulses compensates for the lower deposition between pulses. The latter will be investigated in this chapter. Other interesting effects of pulsing that appear will of course also be investigated. The pulse parameters that we will vary are the pulse length and the duty cycle of the wave. The focus will be mainly on the effect of pulsing on the deposition rate of silane.

4.2 Pulsed power input

The same model is used as for the hydrogen model of chapter 2. The pulsed input power used by S. Hübner is simulated using a square wave with the same pulse length and frequency as he used [15]. The length of the pulse is 6.15 ms and the wave has a frequency of 81 Hz. The duty cycle of the wave is therefore 50%: half of the time the power is on. It is important to mention that we didn't use a perfect rectangular wave because of computational considerations. The rectangular wave is therefore approximated with a trapezium waveform with very steep slopes and somewhat curved edges (see figure 26). The onset and offset time of the pulse are 7 μs, only 0.11% of the pulse time and the shape of the pulse is therefore very similar to a rectangle. The model crashes when the input power drops to zero. The input power between pulses is therefore not zero, but 0.1 W (≈0.003 % of the pulse power). In order to make a good comparison between the constant power plasma and

pulsed power plasma, the averaged input power should be the same. The amplitude P_p of rectangular pulse should therefore be twice as large, since the power is on only half of the time, so the power during the pulse is 3000W. A figure of the waveform can be found in figure 25. The pressure of the plasma equals 0.8 mbar. It is important to note that Hübner used argon plasma and here a hydrogen plasma is investigated. The two plasmas are quite different, but still interesting to compare.

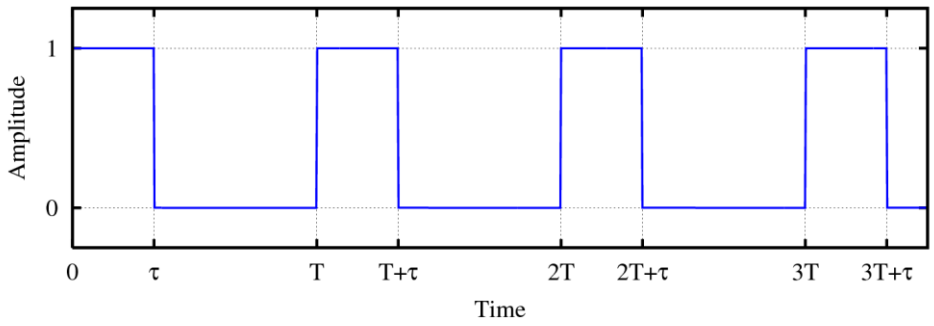

Figure 25.The rectangular waveform. The period is given by T, the pulse length is indicated by τ. [19]

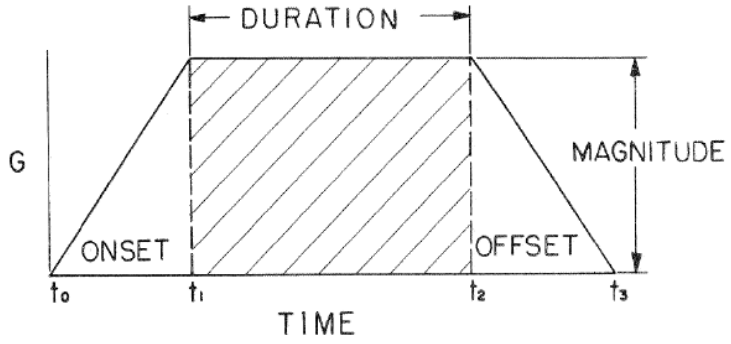

Figure 26. The trapezium waveform. If the slopes are chosen very steep one will approximate a rectangular wave. The onset and offset time are indicated as t_1 and t_3 , both are 7 μs. The duration is the time that the pulse keeps its maximum value, here 6.15 ms. The magnitude equals 3000W [20].

4.3 Results and discussion

4.3.1. Pulsed hydrogen plasma

The results of the pulsed plasma are given in figures below. In figure 27 the electron temperature is shown during the time of three pulses. In the beginning of the pulse the temperature rises quickly to 3.68 eV and then drops quickly to equilibrium at 1.85 eV, slightly higher than the constant power electron temperature of 1.7 eV. At the end of the pulse the electron temperature collapses and slowly rises until the next pulse. Similar behavior is observed in the measurements of S. Hübner carried out on argon plasma. His results are shown in figure 29. The rise of the electron temperature after the end of the pulse is however not observed by Hübner. The reason for this behavior has probably to do with the fact that the input power does not decrease to zero (power can't drop to

zero because the model will crash). A very small group of electrons will absorb the small input power and this will increase their electron temperature. Meanwhile, the energy loses of this small group of electrons and the electron production are very small (since the low value of the electron temperature), contributing to this growth. A higher input power between the pulses leads to a stronger increase of electron temperature providing another clue for this explanation (see figure 28).

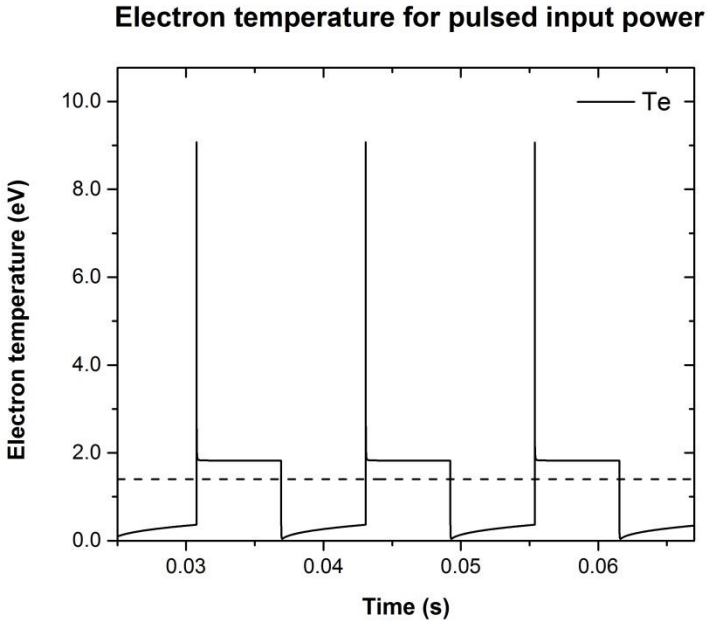

Figure 27. The electron temperature is shown during the time of three pulses. The dashed line depicts the temperature for constant power. In the beginning of the pulse the temperature rises quickly to 9.1 eV and drops quickly to equilibrium (1.85 eV). At the end of the pulse the electron temperature collapses and slowly rises until the next pulse.

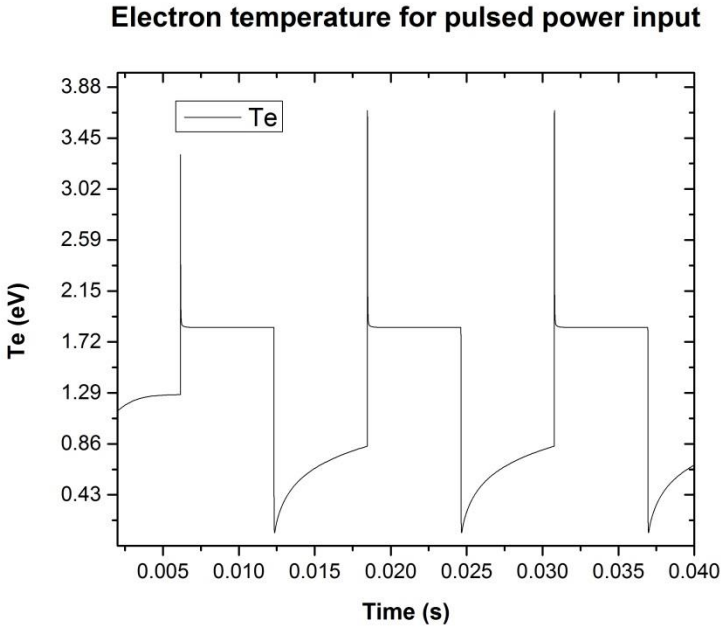

Figure 28. The electron temperature is shown during the time of three pulses. In the beginning of the pulse the temperature rises explosively to 3.68 eV and drops quickly to equilibrium (1.85 eV).

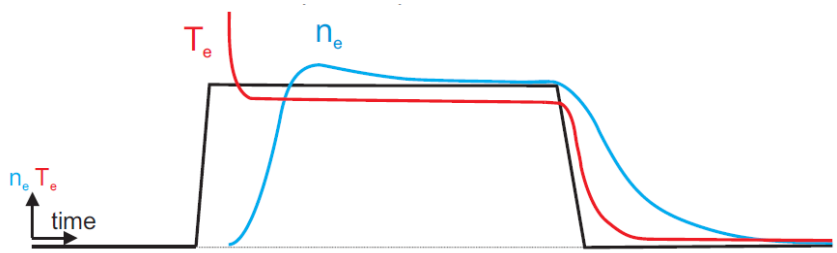

Figure 29. Schematic representation of the electron density and temperature as function of time measured by S. Hübner. The black line depicts the pulse. [15]

The reaction of the electron density to the pulse can be seen in figure 30. The shape of the electron density is pretty similar to the pulse. The overshoot right after the start of the pulse, observed in the measurements, is not found in the modeled results. However the trends are roughly the same. The electron density is during the pulse $2.3 \cdot 10^{17}$ compared to $9.6 \cdot 10^{16}$ for constant power.

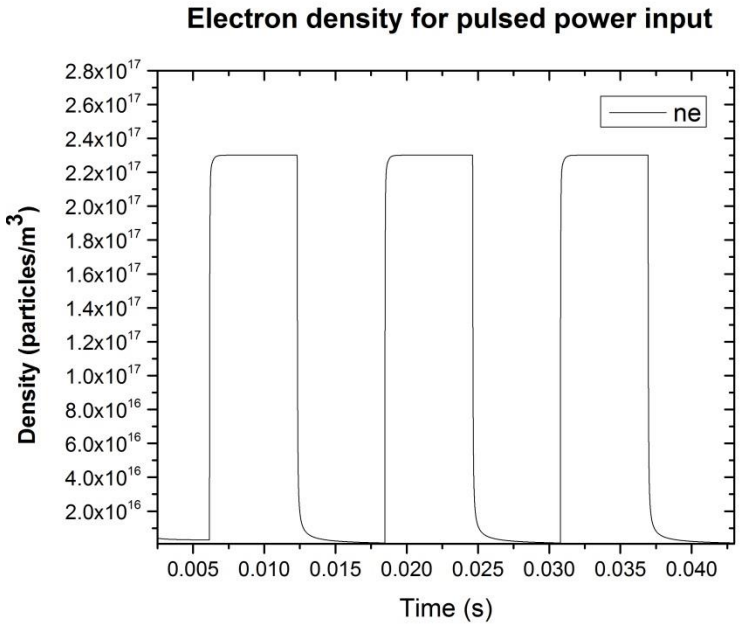

Figure 30.The electron density as function of time. The time of three pulses is shown in the figure. The electron density rises quickly when the pulse starts and reached equilibrium until the pulse stops, then the electron density collapses three orders of magnitudes.

As expected, the pulsed power global model takes considerably more computational time (1000 iterations for one pulse) than the constant power model (200 iterations till convergence). The global model approach turns out to be a good choice: if the 2D model would take 5 times longer it would have taken more than ten weeks to see one pulse!

4.3.2 Pulsed hydrogen-silane plasma

For the hydrogen-silane plasma the same pulsed input power is used as described in the previous section. The influence of pulsing on the deposition rate is investigated in this section. In order to do so, the deposition rate of a constant power is compared with the deposition rate of pulsed power. The average input power is the same for both inputs. The effect of the pulse on the electrons is displayed in the two next figures. The electron temperature does not show the same sharp overshoot as the temperature in the hydrogen model did. This is possibly a consequence of the fact that the electron density does not fall to zero between two pulses. In this way the sudden input power is shared by a larger group of electrons resulting in less energy per electron and so a smaller increase of electron temperature at the beginning of the pulse. The electron density reacts significantly slower to the pulse than the electrons did in the hydrogen model (see figure 32).

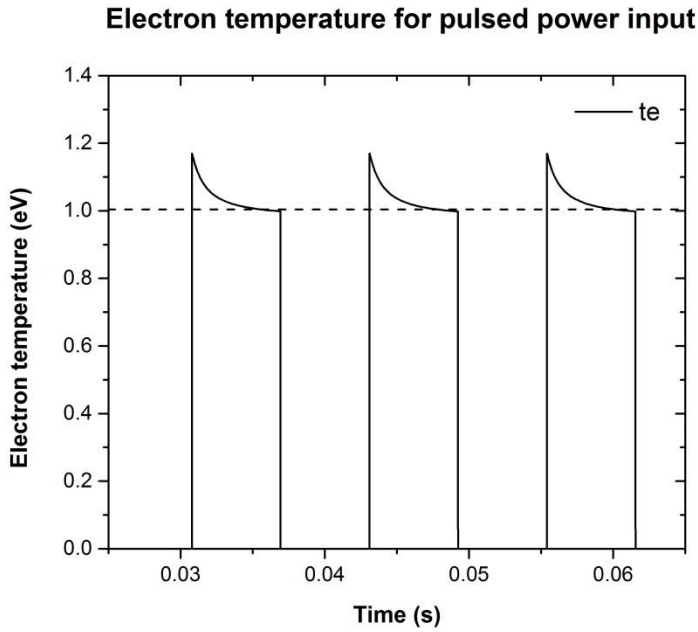

Figure 31. The electron temperature is shown during the time of three pulses. The dashed line indicates the electron temperature for constant power. In the beginning of the pulse the temperature rises explosively to 1.17 eV and drops slowly and then collapses at the end of the pulse. As one can see the electron temperature does not show a major increase during the pulse.

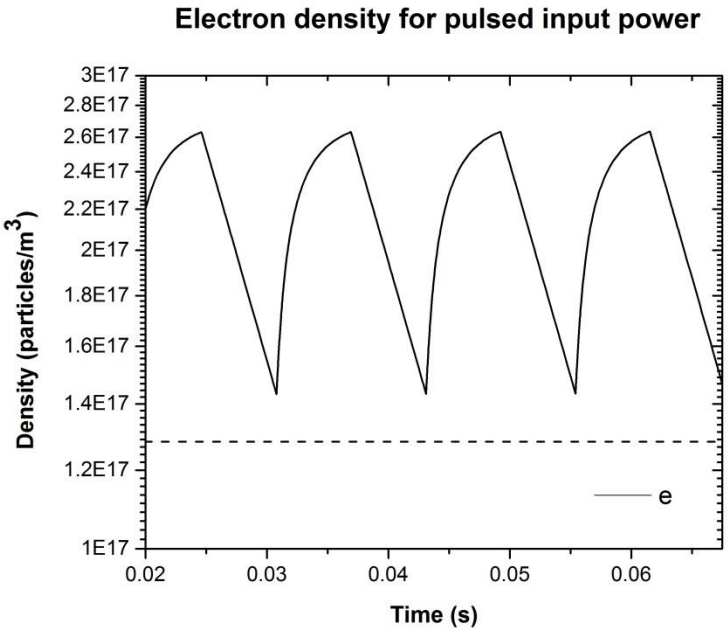

Figure 32. The electron density during four pulses. The dashed line indicates the electron density for constant power. The electron density rises slower than the electron temperature and does not collapse as fast as the electron temperature at the end of the pulse. Surprisingly the density does not go to zero, because the decrease of the electron density takes too long, so the next pulse is already starting before it reaches zero.

The effect of pulsing on the deposition rate is very interesting. The reaction of the deposition rate on the pulse is given in figure 33. The deposition rates rise at the start of the pulse due to a sudden increase in radical production. At the end of the production the number of radicals slowly decreases and the deposition rate drops. None of the rates go to zero between two pulses; apparently the radicals are not totally lost on these time scales. When the average deposition rate for pulsed input power is calculated and compared to the constant power deposition rate we see a slight decrease in deposition rate for most radicals. SiH_3 and Si_2H_5 show slight decrease in deposition rate, 24 and 15 percent respectively. SiH_2 shows however a small increase of 11 percent. The main reason why we expect an increase in deposition during a pulse, is the fact that the higher power results in an electron temperature peak at the beginning of the pulse and a higher electron temperature during the pulse, which causes many reaction rates to grow exponentially. Many of the reaction that depend on the electron temperature are namely of the form

$$Reaction\ rate = a\ T_e^b e^{-\frac{c}{T_e}}, \tag{29}$$

where a and c are positive constants, b is a constant with a value smaller than one. An increase of the electron temperature causes therefore a much larger increase in the reaction rate. This effect might compensate for the lower reaction rate between the pulses. In this case the electron temperature does however not show a large peak at the start of the pulse neither does it show a major increase of temperature during the pulse. As a consequence pulsing could not lead to a larger average deposition rate. If the electron density goes to nearly zero between pulses, the electron temperature might show a larger increase. In order to accomplish this, the time between two pulses should be longer: the duty cycle should be decreased or a longer pulse length. Both are investigated and presented on the next pages.

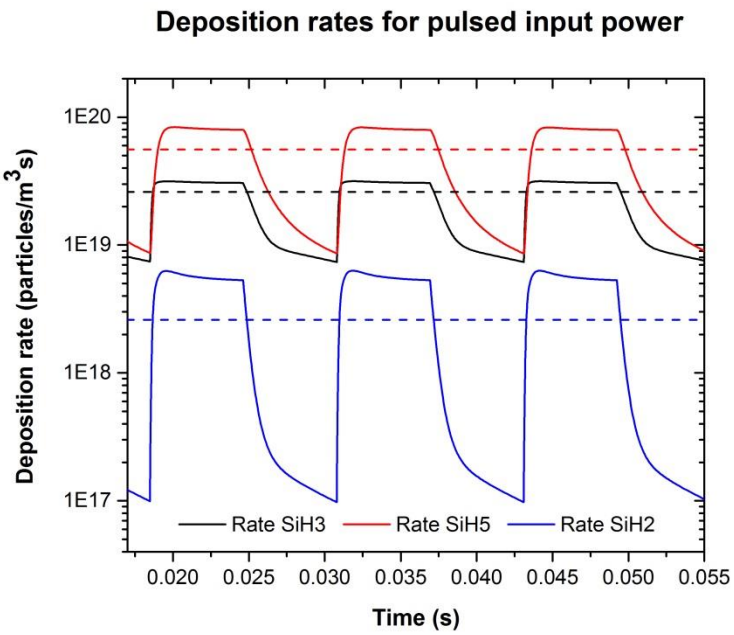

Figure 33.The deposition rates as function of time. The deposition rates rise at the start of the pulse due to a sudden increase in radical production. At the end of the production the number of radicals slowly decreases and the deposition rate drops. The dashed lines indicate the deposition rate for constant power. The pressure of the plasma equals 0.8 mbar.

Other pulse lengths than 6.15 ms are also applied. A square wave with 3 ms pulse duration, 3000 W power during the pulse and a duty cycle of 50% is applied. Besides a shorter pulse length we also applied a longer pulse length of 12 ms, 3000W power during the pulse and a duty cycle of 50%. In the next picture the deposition rate is plotted as function of the pulse length. The deposition rate is slightly increasing as function of pulse length. From the figure it follows that higher pulse duration leads to a higher deposition rate. This is what we expected earlier. A constant input power leads however to an even higher deposition rate, suggesting that pulsing does not improve deposition. A reason for this behavior should be found in the behavior of the densities of the radicals. According to the model, the majority of the radicals are formed in reactions with atomic hydrogen (reactions 21, 22 and 25 of table 10). Atomic hydrogen is mainly formed by dissociation of molecular hydrogen. This dissociation is caused by electron collisions, but since the electron density does respond relatively slowly to the pulse (see figure 32), the electron density is during large part of the pulse relatively low. The latter results in a relatively low hydrogen production and therefore in a low radical production and deposition rate during a large part of the pulse.

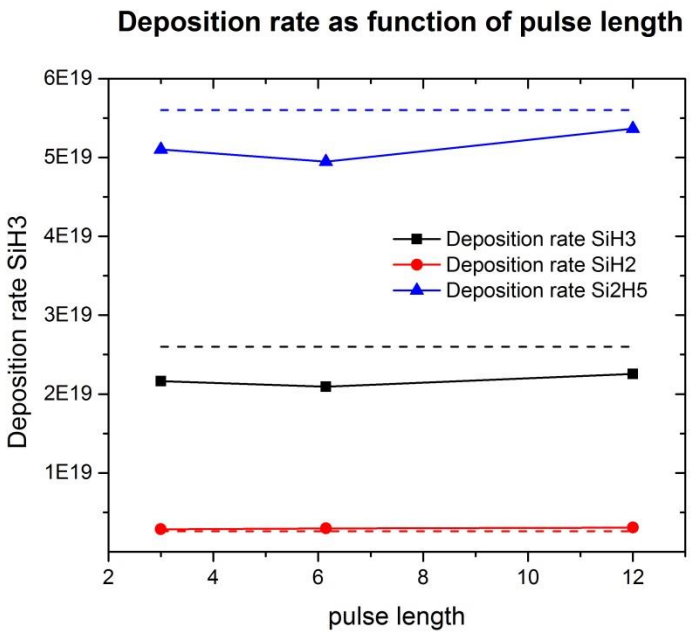

Figure 34.Deposition rate as function of pulse duration. The dashed line depicts the deposition rate for constant power. A very slight increase of deposition is observed for increased pulse length.

Besides pulse duration we can also change the duty cycle of the pulse. Changing the duty cycle will automatically transform the square wave into a rectangular wave, since the power-on time is no longer equal to the power-off time. Duty cycles of 25% and 75% are applied. The power during the power-on time is chosen in such a way that the time averaged power of the wave equals the constant power input. In this case the power during the pulse is 6000 W and 2000 W respectively. The effect of the different duty cycles is displayed in figure 36. The graph shows for SiH_3 and Si_2H_5 a slight increase of deposition rate as function of duty cycle and for SiH_2 a slight decrease. A shorter pulse with higher power results in a more intense pulse leading to higher deposition. During the pulse of the 25% duty cycle an electron density is reached of $5.7 \cdot 10^{17}$ electrons per m^3, compared to $1.7 \cdot 10^{17}$ electrons per m^3 for the 75% duty cycle. Other species showed also higher densities for lower duty cycles. The electron temperature has however similar values for both duty cycles, both are approximately 1eV. The practically constant electron temperature does not lead to exponential growth of reaction rates during pulses and despite of the higher densities, the additional deposition does not reach high enough values to compensate for the lower deposition between the pulses. The graph in figure 23 already showed a clue for this conclusion. This figure shows a nonlinear increase of the deposition rate as function of power, indicating that a non-uniform distribution of the power over time does not lead to an equal average deposition, but to a lower deposition. More fundamental answers are provided by graph 35. This graph shows the relation between the electron temperature and the input power. Earlier we assumed an increase of electron temperature with increase of power. During pulses, the power is higher resulting in higher electron temperatures and this lead to exponential growth of many reaction rates. However, according to graph 35, the electron temperature does not increase with power; it decreases. This is a surprising result, that provides us with the more fundamental reasons why pulsing has not led to higher average deposition in this model. Apparently electrons lose more energy than they gain when power is increased. In Plasimo the electron losses are not very easy to analyze. The elastic collisions of

electrons with hydrogen could be excluded, but there has been no time to investigate all the ionization and dissociation reactions.

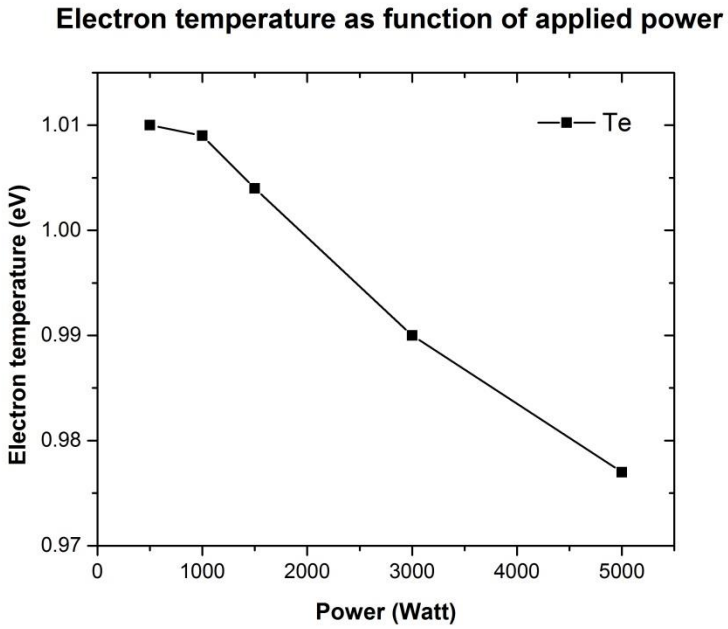

Figure 35.The electron temperature decreases as function of input power. Probably the more fundamental reason why pulsing does not work in this model. The results are obtained with constant power at a pressure of 0.8 mbar.

Besides lower average deposition rates, lower average densities of SiH_3 and Si_2H_5 are observed. The density of SiH_2 is however found to be higher. Concerning the production and destruction of the radicals the following results are found: the main production mechanism of SiH_3 and Si_2H_5 are the reaction of atomic hydrogen with silane (reaction 21) and the reaction of atomic hydrogen with Si_2H_6 (reaction 22) respectively. The main loses caused by the recombination of SiH_3 with atomic hydrogen (reaction 25) and the recombination of two Si_2H_5 molecules (reaction 29). Both lose mechanism produce SiH_2 leading to the opposite behavior of this species: an increase with decreasing duty cycle.

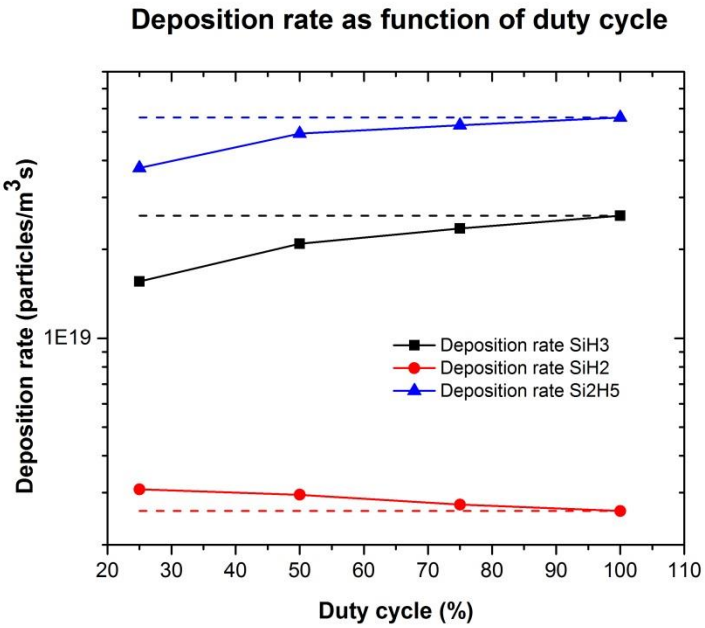

Figure 36.Deposition rate as function of duty cycle. The dashed lines indicate the deposition rate for constant power. For SiH_3 and Si_2H_5, a slight increase is observed as the duty cycle increases. SiH_2 shows the opposite behavior and decreases slightly. The reason for this behavior is the fact that the reaction responsible for the main loses of SiH_3 and Si_2H_5 both produce SiH_2.

4.4 Conclusion

In this chapter pulsed input power is applied to both hydrogen and hydrogen-silane plasma. The pulsed power is simulated as a rectangular wave with different pulse lengths and duty cycles. Since many reaction rates depend exponentially on the electron temperature, it was expected that the electron temperature peak at the start of the pulse and the higher value throughout the pulse compensate for the time between pulses and lead to a higher average deposition. The most significant finding is however that no form of rectangular pulsing leads to a higher deposition rate. The shorter the pulse time of the square wave, the higher the electron density remains and the lower the electron temperature peaks at the start of each pulse. As a consequence a lower deposition rate is observed. A lower duty cycle resulted in a significant higher electron temperature and therefore in more reactive plasma, however average densities and deposition rates are found to be lower than for constant power. The exception to this behavior is the radical $\mathrm{SiH_2}$, the deposition of this species increases with decreasing of the duty cycle. The reason why pulsing did not lead to increased deposition rates, has to do with the fact that the electron temperature showed no major increases during the pulse. As a consequence reaction rates did not grow exponentially and no higher deposition rates were established. A plot of the electron temperature as function of power revealed the reasons for the unexpected behavior. According to the graph, the electron temperature decreases with an increase of the power input. The assumption made in the beginning seems to be false and therefore no increase of deposition rate is to be expected. For further research it is interesting to take a closer look at the reaction of the electron temperature to the applied power. What is the reason for the decrease? Is this same behavior also found in experiments or is it just a feature of this model?

References

[1] S. Rahimi, *Modelling of Microwave induced deposition plasmas (thesis)*, Eindhoven University of technology, 2014, ISBN: 978-90-386-3589-7.

[2] Sumio Ashida, C. Lee, and M. A. Lieberman, *Spatially averaged (global) model of time modulated high density argon plasmas,* Journal of Vacuum Science & Technology, vol. 13, no. 5, 1995.

[3] The Plasimo team of the EPG-group of Eindhoven University of technology, *Plasimo user guide*, Eindhoven University of technology, 2015.

[4] R. Zorat, J. Goss, D. Boilson and D. Vender, *Global model of a radiofrequency H2 plasma in DENISE*, Plasma Sources Sci. Technol, no.9, 1999.

[5] V.A. Godyak, *Soviet Radio Frequency Discharge Research p. 88*, Delphic associates incorporated, 1986.

[6] R. K. Janev, W. D. Langer, Douglass E. Post Jr. and Kenneth Evans Jr. *Elementary Processes in Hydrogen-Helium Plasmas*. Springer Series on Atomic, Optical, and Plasma Physics. Springer, 1987.

[7] Mark J. Kushner. *‚A model for the discharge kinetics and plasma chemistry during plasma enhanced chemical vapor deposition of amorphous silicon*, Journal of Applied Physics, 63(8), 1988.

[8] Zahoor Ahmad and W J Goedheer. *Optimization and characterization of a pilot-psi cascaded arc with non-lte numerical simulation of ar, h2 gases*, Plasma Sources Science and Technology, 18(1), 77, 2009.

[9] J. Perrin, O. Leroy, and M. C. Bordage. *Cross-sections, rate constants and transport coefficients in silane plasma chemistry*, Contributions to PlasmaPhysics, 36(1), 3–49, 1996.

[10] Ellen Meeks, Richard S. Larson, Pauline Ho, Christopher Apblett, Sang M. Han, Erik Edelberg, and Eray S. Aydil. *Modeling of sio2 deposition in high density plasma reactors and comparisons of model predictions with experimental measurements*, Journal of Vacuum Science & Technology A, 16(2), 1998.

[12] Olivier Leroy, GÃlrard Gousset, Luis Lemos Alves, Jerome Perrin, and Jacques Jolly. *Two-dimensional modelling of-radio-frequency discharges for a-si: H deposition*, Plasma Sources Sci. Technol., 7(3), 1998.

[13] G Gousset A Salabas and L L Alves. *Two-dimensional fluid modelling of charged particle transport in radio-frequency capacitively coupled discharges*, Plasma Sources Sci. Technol., 11(4), 2002.

[14] G. J. M. Hagelaar, K. Hassouni, and A. Gicquel. *Interaction between the electromagnetic fields and the plasma in a microwave plasma reactor,* Journal of Applied Physics, 96(4), 1819–1828, 2004.

[15] S. Hübner, Poly-diagnostic study of low pressure microwave plasmas (thesis), Eindhoven University of technology, 2013.

[16] W. Soppe, H. Rieffe, and A.Weeber. *Bulk and surface passivation of silicon solar cells accomplished by silicon nitride deposited on industrial scale by microwave pecvd*, Prog. Photovolt: Res. Appl., 13(7), 551, 2005.

[17] J. Perrin, O. Leroy, and M. C. Bordage. *Cross-sections, rate constants and transport coefficients in silane plasma chemistry,* Contributions to Plasma Physics, 36(1), 3–49, 1996.

[18] R. Serway, *Physics for Scientists and Engineers with modern physics*, 3rdEd, Saunders College Publishing, 1990.

[19] https://commons.wikimedia.org/wiki/File:Dutycycle.svg, visited on 23-6-2015

[20] G. Holcomb, *Human Experiments to Determine Human Tolerance to Landing Impact in Capsule Systems*, Ballistic Missile and Space Technology. vol. I, D. LeGalley, Ed., ed New York, New York: Academic Press, 1960.

[21] J.O. Hirschfelder, C.F. Curtiss, R.B. Bird, *The Molecular Theory of Gases and Liquids*, Wiley-Interscience, 1964, ISBN-13: 978-0471400653.

[22] Dijk J. van, Peerenboom K.S.C., Jimenez-Diaz M., Mihailova D.B. and Mullen J.J.A.M. van der, *The plasma modelling toolkit Plasimo*, Journal of Physics D: Applied Physics, 42(19), 194012-1/14, 2009.